

Acoustic Waveform Inversion with Image-to-Image Schrödinger Bridges

A.S. Stankevich*, I.B. Petrov

Moscow Institute of Physics and Technology, info@mipt.ru

April 30, 2025

Abstract

Recent developments in application of deep learning models to acoustic Full Waveform Inversion (FWI) are marked by the use of diffusion models as prior distributions for Bayesian-like inference procedures. The advantage of these methods is the ability to generate high-resolution samples, which are otherwise unattainable with classical inversion methods or other deep learning-based solutions. However, the iterative and stochastic nature of sampling from diffusion models along with heuristic nature of output control remain limiting factors for their applicability. For instance, an optimal way to include the approximate velocity model into diffusion-based inversion scheme remains unclear, even though it is considered an essential part of FWI pipeline. We address the issue by employing a Schrödinger Bridge that interpolates between the distributions of ground truth and smoothed velocity models. Thus, the inference process that starts from an approximate velocity model is guaranteed to arrive at a sample from the distribution of reference velocity models in a finite time. To facilitate the learning of nonlinear drifts that transfer samples between distributions and to enable controlled inference given the seismic data, we extend the concept of Image-to-Image Schrödinger Bridge (I²SB) to conditional sampling, resulting in a conditional Image-to-Image Schrödinger Bridge (cI²SB) framework for acoustic inversion. To validate our method, we assess its effectiveness in reconstructing the reference velocity model from its smoothed approximation, coupled with the observed seismic signal of fixed shape. Our experiments demonstrate that the proposed solution outperforms our reimplementation of conditional diffusion model suggested in earlier works, while requiring only a few neural function evaluations (NFEs) to achieve sample fidelity superior to that attained with supervised learning-based approach. The supplementary code implementing the algorithms described in this paper can be found in the repository https://github.com/stankevich-mipt/seismic_inversion_via_I2SB

1 Introduction

The general purpose of seismic inversion procedures is to reveal the properties of the subsurface medium given results from non-destructive scanning [1]. Typical inverse problems encountered in seismology are ill-posed and underconstrained, as the data coverage is fundamentally limited due to the nature of the scanning setup. Thus, they are usually solved numerically using various physics-based approximations of continuous media and regularization techniques that guarantee the existence of a solution ([2], [3]).

A significant part of seismic inversion studies is performed in the acoustic approximation. The dynamics of the acoustic medium is governed by a second-order partial-differential equation (PDE) parameterised by a single function of acoustic velocity [4]. As such, the process of seismic scanning is formulated as an initial-boundary value problem for the acoustic PDE. Inverting the data of acoustic seismic scanning involves recovering the spatial distribution of the medium's velocity using the waveform data recorded at the location of signal receivers.

Recent advances in signal processing with deep learning algorithms have encouraged researchers to actively investigate data-driven approaches to seismic inversion [5], [6]. A common strategy for supervised frameworks is to employ convolutional neural networks that take either preprocessed ([7]–[9]) or raw ([10]–[12]) waveform data as input and map it directly to corresponding velocity images. The training data for such models in the majority of cases is handcrafted – finite-difference computational engines emulate the dynamics of acoustic media parameterised by manually generated velocity fields, obtaining matching seismogram-impedance image pairs.

Diffusion models ([13], [14]) have shown themselves as a promising tool for solving imaging inverse problems. Namely, the diffusion model generation process could be altered in order to perform posterior sampling conditioned on measurements using Bayesian inference [15]. This aforementioned feature requires evaluation of

*stankevich.as@phystech.edu; Corresponding Author

the conditional score, a task that can be done either in zero-shot fashion by imposing a statistical hypothesis on the structure of observed data ([16]–[18]), or by internal means of deep learning models ([19], [20]). Regardless of the specifics, neural network here could be viewed as an implicit prior disentangled from the data acquisition model.

To date, such insight has already been employed by several researchers on the topic of deep-learning applications in seismic inversion ([21]–[23]). Since the procedure of waveform inversion commonly progresses from coarse to fine resolution and is known to be sensitive to initial approximation, researchers naturally gravitate towards conditioning models on smoothed velocity models as auxiliary input. However, to the best of our knowledge, conditioning methods present in the literature on acoustic inversion with diffusion-based models are so far purely heuristic. The goal of this paper is to demonstrate a data-driven seismic inversion technique that incorporates smoothed velocity models into the diffusion-based workflow on a theoretical basis. Our contribution is as follows:

- We have developed a novel acoustic waveform inversion scheme based on the problem statement described in the conditional Diffusion Schrödinger Bridge paper (cDSB, [24]). To facilitate the process of generative model building, we have adapted the training pipeline proposed for a specific case of Schrödinger Bridge problem statement described by Liu et al [25] towards conditional simulation, resulting in a conditional Image-to-Image Schrödinger Bridge (cI²SB)
- We have designed an end-to-end training procedure similar to classifier-free diffusion guidance [19] that allows our model to learn nonlinear drifts for both conditional and unconditional settings within the scope of the same framework (fig. 1). We have demonstrated that model trained in this way achieves a sample diversity/fidelity tradeoff, which can be controlled through a mixing weight parameter.
- We have assessed the performance of the proposed scheme using the OpenFWI data collection [26]. Our experiments have shown that the developed method outperforms several solutions introduced in previous works on the subject.

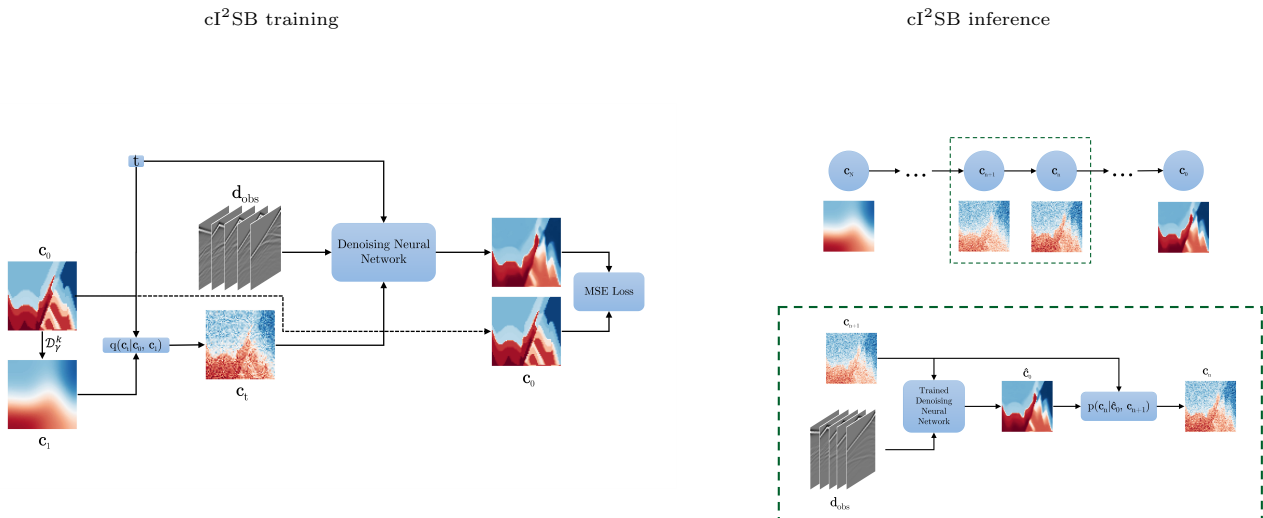


Figure 1: Conditional Image-to-Image Schrödinger Bridge in application to acoustic seismic inversion

2 Background

2.1 Acoustic Waveform Inversion with Deep Learning

Consider a continuous medium governed by the 2D acoustic wave equation

$$\Delta \mathbf{p} - \frac{1}{\mathbf{c}_0^2} \frac{\partial^2 \mathbf{p}}{\partial t^2} = \mathbf{s} \quad (1)$$

Here Δ is the 2D Laplace operator, $\mathbf{p}(x, y, t)$ is the pressure field, $\mathbf{s}(x, y, t)$ is the source function, and $\mathbf{c}_0(x, y)$ is the velocity field. The conventional regularized full waveform inversion (FWI, [27]) problem statement is

formulated as an optimization task

$$\min_{\mathbf{c}_0} J(\mathbf{d}_{\text{model}}, \mathbf{d}_{\text{obs}}) + \lambda R(\mathbf{c}_0) \quad \text{s.t.} \quad \mathbf{d}_{\text{model}} = F(\mathbf{c}_0) \quad (2)$$

where J measures the discrepancy between modelled $\mathbf{d}_{\text{model}}$ and observed \mathbf{d}_{obs} seismic data, F is the forward modelling operator, and $R(\mathbf{c}_0)$ is the regularization term scaled by the λ multiplier. The purpose of regularization is to ensure the existence of a solution. In other words, the goal of full waveform inversion is to estimate the value of "pseudoinverse" of F applied to the observed data

$$\mathbf{c}_0^* = \hat{F}^{-1}(\mathbf{d}_{\text{obs}}) \quad (3)$$

Supervised learning-based approaches to acoustic waveform inversion seek $\hat{F}_{\boldsymbol{\theta}}^{-1}$ – a parametric approximation of \hat{F}^{-1} . The implementation of $\hat{F}_{\boldsymbol{\theta}}^{-1}$ commonly involves convolutional neural networks, as both seismograms and 2D velocity models resemble multichanneled images. The tuning of parameters $\boldsymbol{\theta}$ is carried out using gradient optimization on a training dataset, which contains paired instances of velocity models $\mathbf{c}_{\text{train}}^i$ and corresponding observed data $\mathbf{d}_{\text{train}}^i$. Once the parameter fitting is done, $\mathbf{c}_{\text{test}}^i = \hat{F}_{\boldsymbol{\theta}^*}^{-1}(\mathbf{d}_{\text{test}}^i)$ yields the reconstructed velocity model for seismogram $\mathbf{d}_{\text{test}}^i$.

2.2 Score-based Generative Modelling (SGM)

SGM [15] is a framework for generative modelling which considers the morphing process of probability distributions from the perspective of solutions to stochastic differential equations (SDEs). The main object of interest for SGM is a forward SDE of the form

$$d\mathbf{x} = \mathbf{f}(\mathbf{x}, t) dt + \sqrt{\beta_t} d\mathbf{w}, \quad \mathbf{x} \in \mathbb{R}^d, \quad t \in [0, 1] \quad (4)$$

With the proper choice of β_t and f_t - the latter has to be linear on \mathbf{x} - the terminal distributions of noising equation approaches standard Gaussian regardless of the initial distribution, i.e., $\mathbf{x}_1 \sim \mathcal{N}(0, 1) \forall \mathbf{x}_0 \sim p_{\text{data}}$. A notable property of the equation (4) is the existence of its time-reversal [28], defined by

$$d\mathbf{x} = -[\mathbf{f}(\mathbf{x}, t) - \beta(t)\nabla_{\mathbf{x}_t} \log p_t(\mathbf{x}_t)] dt + \sqrt{\beta(t)} d\bar{\mathbf{w}} \quad (5)$$

Forward and backward SDEs share the same marginal probability densities, since path measures induced by equations (4) and (5) are equal almost surely. Thus, it is possible to construct generative process by means of denoising score matching [29]

$$\min_{\boldsymbol{\theta}} \|s_{\boldsymbol{\theta}}(\mathbf{x}_t, t) - \sigma_t \nabla \log p(\mathbf{x}_t, t | \mathbf{x}_0)\| \quad (6)$$

Here the output of parametric model $s_{\boldsymbol{\theta}}(\mathbf{x}_t, t)$ is regressed towards the score $\nabla_{\mathbf{x}_t} \log p(\mathbf{x}_t, t | \mathbf{x}_0)$ of the forward process (4), which can be effectively computed at runtime. Once trained, the score estimator can be substituted into the discretization of (5) in place of the unknown term $\nabla_{\mathbf{x}_t} \log p_t(\mathbf{x}_t)$, resulting in recursive procedure for sampling from the considered distribution.

2.3 Schrödinger Bridge (SB)

Dynamic SB expression ([30]–[32]) describes an entropy-regularized optimal transport problem for two different distributions p_{data} and p_{prior} on a finite time interval $t \in [0, T]$

$$\min_{\mathbb{Q} \in \mathcal{P}(p_{\text{data}}, p_{\text{prior}})} D_{\text{KL}}(\mathbb{Q} || \mathbb{P}) \quad (7)$$

In the statement above \mathbb{Q} belongs to a set of path measures having p_{data} and p_{prior} as its marginal densities, and \mathbb{P} is a reference measure. If \mathbb{P} is a path measure associated with stochastic process (4), the optimality condition for (7) is provided by a set of PDEs coupled through their boundary conditions [33], [34]. To wit, let $\Psi(\mathbf{x}_t, t), \hat{\Psi}(\mathbf{x}_t, t) \in C^{2,1}(\mathbb{R}^d, [0, T])$ be the solution of the following system of equations

$$\frac{\partial \Psi(\mathbf{x}, t)}{\partial t} = -\nabla_{\mathbf{x}} \Psi^T \mathbf{f} - \beta_t \frac{1}{2} \Delta \Psi \quad (8a)$$

$$\frac{\partial \hat{\Psi}(\mathbf{x}, t)}{\partial t} = -\nabla_{\mathbf{x}} \cdot (\hat{\Psi} \mathbf{f}) + \beta_t \frac{1}{2} \Delta \hat{\Psi} \quad (8b)$$

$$\text{s.t.} \quad \Psi(\mathbf{x}, 0) \hat{\Psi}(\mathbf{x}, 0) = p_{\text{data}} \quad \Psi(\mathbf{x}, T) \hat{\Psi}(\mathbf{x}, T) = p_{\text{prior}} \quad (8c)$$

In this case, the solution to optimization problem (7) can be expressed by the path measure of either the forward (9a), or, equivalently, the backward (9b) SDEs

$$d\mathbf{x}_t = [\mathbf{f}_t + \beta_t \nabla_{\mathbf{x}_t} \log \Psi(\mathbf{x}_t, t)] dt + \sqrt{\beta_t} d\mathbf{w}_t \quad (9a)$$

$$d\mathbf{x}_t = [\mathbf{f}_t - \beta_t \nabla_{\mathbf{x}_t} \log \hat{\Psi}(\mathbf{x}_t, t)] dt + \sqrt{\beta_t} d\bar{\mathbf{w}}_t \quad (9b)$$

Similarly to SGM, path measures induced by stochastic processes (9a) and (9b) are equal almost surely. Equations (9) can be viewed as a nonlinear generalization of forward and backward SGM equations (4) (5), since the inclusion of nonlinear drift allows diffusion to transfer samples beyond Gaussian priors on a finite time horizon.

2.4 Conditional Diffusion Schrödinger Bridge

Consider the discrete equivalent of noising process (4) represented by a Markov chain $\mathbf{x}_{0:N} = \{\mathbf{x}_k\}_{k=0}^N \in \mathcal{X} = (\mathbb{R}^d)^{N+1}$ with joint density

$$p(\mathbf{x}_{0:N}) = p_0(\mathbf{x}_0) \prod_{k=0}^{N-1} p_{k+1|k}(\mathbf{x}_{k+1}|\mathbf{x}_k) \quad (10)$$

where $p_0 = p_{\text{data}}$ and $p_{k+1|k}$ are Markov transition densities, with $p_{k+1}(\mathbf{x}_{k+1}) = \int p_{k+1|k}(\mathbf{x}_{k+1}|\mathbf{x}_k) p_k(\mathbf{x}_k) d\mathbf{x}_k$. De Bortoli et al. [35] formulated the dynamic Schrödinger Bridge problem for forward density $p(\mathbf{x}_{0:N})$ of the noising chain (10).

$$\pi^* = \arg \min_{\pi} \{D_{\text{KL}}(\pi || p(\mathbf{x}_{0:N})) : \pi_0 = p_{\text{data}}, \pi_N = p_{\text{prior}}\} \quad (11)$$

that admits a solution in form of Iterative Proportional Fitting procedure adapted towards score matching ideas. Now, suppose that we are interested in sampling from a posterior distribution

$$p(\mathbf{x}|\mathbf{y}^{\text{obs}}) \propto p_{\text{data}}(\mathbf{x})g(\mathbf{y}^{\text{obs}}|\mathbf{x})$$

using an $N+1$ - step discrete Schrödinger Bridge, assuming that it is possible to sample $(\mathbf{x}, \mathbf{y}) \sim p_{\text{data}}(\mathbf{x})g(\mathbf{y}|\mathbf{x})$. A straightforward approach would be to consider the SB problem (11) with $p_{\text{data}}(\mathbf{x})$ replaced by the posterior $p(\mathbf{x}|\mathbf{y}^{\text{obs}})$, i.e.

$$\pi^* = \arg \min_{\pi} \{D_{\text{KL}}(\pi || p_{\mathbf{y}^{\text{obs}}}) : \pi_0 = p(\cdot|\mathbf{y}^{\text{obs}}), \pi_N = p_{\text{prior}}\} \quad (12)$$

where $p_{\mathbf{y}^{\text{obs}}}(\mathbf{x}_{0:N}) := p(\mathbf{x}_0|\mathbf{y}^{\text{obs}}) \prod_{k=0}^{N-1} p_{k+1|k}(\mathbf{x}_{k+1}|\mathbf{x}_k)$ is the forward noising process. The former, however, is explicitly dependent on $p(\mathbf{x}_0|\mathbf{y}^{\text{obs}})$, which is intractable under our assumptions.

This complication can be addressed by solving an amortized problem instead. Let $p_{\text{join}}(\mathbf{x}, \mathbf{y}) = p_{\text{data}}(\mathbf{x})g(\mathbf{y}|\mathbf{x}) = p(\mathbf{x}|\mathbf{y})p_{\text{obs}}(\mathbf{y})$, and $p_{\text{jprior}}(\mathbf{x}, \mathbf{y}) = p_{\text{prior}}(\mathbf{x})p_{\text{obs}}(\mathbf{y})$ where $p_{\text{obs}}(\mathbf{y}) = \int p_{\text{data}}(\mathbf{x})g(\mathbf{y}|\mathbf{x})d\mathbf{x}$. We are interested in finding the transition kernel $\pi^{\text{cond},*} = (\pi_{\mathbf{y}}^{\text{cond},*})_{\mathbf{y} \in \mathcal{Y}}$ where $\pi_{\mathbf{y}}^{c,*}$ defines a distribution on $\mathcal{X} = (\mathbb{R}^d)^{N+1}$ for each $\mathbf{y} \in \mathcal{Y}$ satisfying

$$\pi^{\text{cond},*} = \arg \min_{\pi} \{ \mathbb{E}_{\mathbf{y} \sim p_{\text{obs}}} [D_{\text{KL}}(\pi_{\mathbf{y}}^{\text{cond}} || p_{\mathbf{Y}})] : \pi_0^{\text{cond}} \otimes p_{\text{obs}} = p_{\text{join}}, \pi_N^{\text{cond}} \otimes p_{\text{obs}} = p_{\text{jprior}} \} \quad (13)$$

which is an averaged version of (12) over the distribution $p_{\text{obs}}(\mathbf{y})$ of \mathbf{y} . Once $\pi^{\text{cond},*}$ is known, sampling $\mathbf{x}_N \sim p_{\text{prior}}$, then $\mathbf{x}_k|\mathbf{x}_{k+1} \sim \pi_{\mathbf{y},k|k+1}^{\text{cond},*}(\mathbf{x}_k|\mathbf{x}_{k+1})$ for $k = N-1, \dots, 0$ yields $\mathbf{x}_0 \sim p(\mathbf{x}|\mathbf{y})$ given $Y \sim p(\mathbf{y}^{\text{obs}})$

Problem (13) could be reformulated as a SB on extended space, thus, guaranteeing the existence and uniqueness of the SB solution.

Proposition. (Shi et al., [24]) *Consider the following SB problem*

$$\bar{\pi}^* = \arg \min_{\bar{\pi}} \{D_{\text{KL}}(\bar{\pi} || \bar{p}) : s.t. \bar{\pi}_0 = p_{\text{join}}, \bar{\pi}_N = p_{\text{jprior}}\} \quad (14)$$

where $\bar{p}(\mathbf{x}_{0:N}, \mathbf{y}_{0:N}) := p_{\mathbf{y}_0}(\mathbf{x}_{0:N})\bar{p}_{\text{obs}}(\mathbf{y}_{0:N})$ with $\bar{p}_{\text{obs}}(\mathbf{y}_{0:N}) := \prod_{k=0}^{N-1} \delta_{\mathbf{y}_k}(\mathbf{y}_{k+1})$, and $p_{\mathbf{y}_0}$ is the forward process of (12). If $D_{\text{KL}}(\bar{\pi}^* || \bar{p}) < +\infty$, then $\bar{\pi}^* = \pi^{\text{cond},*} \otimes \bar{p}_{\text{obs}}$, where $\pi^{c,*}$ solves (13).

Compared to (12), both distributions p_{jprior} and p_{join} could be sampled analytically, thus, enabling numerical methods of SB problem solving, such as the one introduced in [35].

2.5 Image-to-Image Schrödinger Bridge (I^2SB)

Liu et al. [25] demonstrate that for certain cases of SB problem statement the necessity to solve system (8) could be circumvented altogether. Such conclusion could be drawn from comparison between (8) and Fokker-Plank equation for Ito process (4), yielding an the alternative formulation for (9), with $\nabla_{\mathbf{x}_t} \log \hat{\Psi}(\mathbf{x}_t, t)$ and $\nabla_{\mathbf{x}_t} \log \Psi(\mathbf{x}_t, t)$ as score functions of the following linear SDEs, respectively

$$d\mathbf{x}_t = \mathbf{f}_t(\mathbf{x}_t, t)dt + \sqrt{\beta_t}d\mathbf{w}_t \quad \mathbf{x}_0 = \hat{\Psi}(\cdot, 0) \quad (15a)$$

$$d\mathbf{x}_t = \mathbf{f}_t(\mathbf{x}_t, t)dt + \sqrt{\beta_t}d\hat{\mathbf{w}}_t \quad \mathbf{x}_T = \Psi(\cdot, T) \quad (15b)$$

Hence, if the values $\Psi(\cdot, T)$ and $\hat{\Psi}(\cdot, 0)$ are tractable, nonlinear drift $\nabla_{\mathbf{x}_t} \log \hat{\Psi}$ transporting samples from p_{prior} to p_{data} could be learned as a score of linear SDE, identical to the one present in SGM framework. The former could be achieved by assuming that data distribution is the *Dirac delta* centered at $a \in \mathbb{R}^d$, i.e., $p_{\text{data}}(\cdot, 0) = \delta_a(\cdot)$. In that case,

$$\hat{\Psi}(\cdot, 0) = \delta_a(\cdot) \quad \Psi(\cdot, T) = \frac{p_{\text{prior}}}{\hat{\Psi}(\cdot, T)} \quad (16)$$

Thus, the model under consideration learns a mixture of scores of degenerate distributions centered on the elements of the training dataset. Additionally, the paper [25] derives the analytic posterior for equations (9) given a boundary pair $(\mathbf{x}_0, \mathbf{x}_T)$ under the assumption of $f := 0$. Namely,

$$q(\mathbf{x}_t | \mathbf{x}_0, \mathbf{x}_1) = \mathcal{N}(\mathbf{x}_t; \boldsymbol{\mu}_t(\mathbf{x}_0, \mathbf{x}_1), \Sigma_t) \quad (17a)$$

$$\boldsymbol{\mu}_t = \frac{\bar{\sigma}_t^2}{\bar{\sigma}_t^2 + \sigma_t^2} \mathbf{x}_0 + \frac{\sigma_t^2}{\bar{\sigma}_t^2 + \sigma_t^2} \mathbf{x}_1 \quad \Sigma_t = \frac{\sigma_t^2 \bar{\sigma}_t^2}{\bar{\sigma}_t^2 + \sigma_t^2} \cdot I \quad (17b)$$

where $\sigma_t^2 = \int_0^t \beta_\tau d\tau$ and $\bar{\sigma}_t^2 = \int_t^T \beta_\tau d\tau$ are variances accumulated from two sides of the diffusion bridge. In addition, such posterior marginalizes the recursive posterior sampling in DDPM [13]

$$q(\mathbf{x}_n | \mathbf{x}_0, \mathbf{x}_N) = \int \prod_{k=n}^{N-1} p_{\text{DDPM}}(\mathbf{x}_k | \mathbf{x}_0, \mathbf{x}_{k+1}) d\mathbf{x}_{k+1} \quad (18)$$

The above circumstances facilitate SB-based generative model building, since eq. (17) allows for analytical sampling of \mathbf{x}_t during training, when \mathbf{x}_0 and \mathbf{x}_T are available. Moreover, eq. (18) ensures that running conventional DDPM starting from \mathbf{x}_T during inference induces marginal density of SB paths.

Finally, in the limit of vanishing stochasticity, i.e. $\beta_t \rightarrow 0$, the SDE between $(\mathbf{x}_0, \mathbf{x}_T)$ reduces to optimal transport ODE

$$d\mathbf{x}_t = \mathbf{v}_t(\mathbf{x}_t | \mathbf{x}_0) dt \quad \mathbf{v}_t(\mathbf{x}_t | \mathbf{x}_0) = \frac{\beta_t}{\sigma_t^2} (\mathbf{x}_t - \mathbf{x}_0) \quad (19)$$

which, similarly to probability flow ODE [15], could be utilized for deterministic sampling and likelihood estimation.

3 Problem Statement and Suggested Method

Consider the acoustic FWI problem statement (eqs. (2) and (3)) coupled with additional information provided by a smooth velocity model $\mathbf{c}_{\text{smooth}}$ of the medium under investigation.

$$\begin{cases} \min_{\mathbf{c}_0} J(\mathbf{d}_{\text{model}}, \mathbf{d}_{\text{obs}}) + \lambda R(\mathbf{c}) \\ \text{s.t. } \mathbf{d}_{\text{model}} = F(\mathbf{c}_0), \quad \mathbf{c}_1 = \mathbf{c}_{\text{smooth}} \end{cases} \quad (20)$$

$\mathbf{c}_{\text{smooth}}$ is believed to be reasonably close to ground truth velocity model \mathbf{c}_0^* , yet lacking high-frequency details. Hence, in realistic inversion scenarios $\mathbf{c}_{\text{smooth}}$ is commonly employed as a starting point for nonlinear optimization.

We propose a novel way to utilize such piece of information in context of recently proposed diffusion-based deep learning approach to acoustic waveform inversion. Our method is two-staged: the first stage consists of fitting the parameters of cl^2SB model on training data. Once the optimal set of parameters is found, $\mathbf{c}_0^* = \hat{F}_{\boldsymbol{\theta}^*}^{-1}(\mathbf{d}_{\text{obs}}, \mathbf{c}_{\text{smooth}})$ is obtained by running the inference process of such model.

The transition from I^2SB to cl^2SB proceeds as follows. According to [24], continuous dynamic SB problem statement matching the one described by equation (13) is formulated as

$$\Pi^* = \arg \min_{\Pi} \{D_{\text{KL}}(\Pi | \mathbb{P}) : \Pi \in \mathcal{P}(\mathcal{C}), \Pi_0 = p_{\text{join}}, \Pi_T = p_{\text{prior}}\} \quad (21)$$

where reference measure \mathbb{P} is associated with

$$\begin{cases} d\mathbf{x} = f(\mathbf{x}, t)dt + \sqrt{\beta_t}d\mathbf{w}_t \\ dy = 0 \end{cases} \quad (22)$$

Schrödinger potentials for such dynamics are defined by a set of hyperbolic PDEs coupled with their boundary conditions [36]

$$\frac{\partial \Psi_t(\mathbf{x}|\mathbf{y})}{\partial t} = -\mathbf{f}_t(\mathbf{x}) \cdot \nabla_{\mathbf{x}} \Psi_t^T(\mathbf{x}|\mathbf{y}) - \beta_t \frac{1}{2} \Delta \Psi_t(\mathbf{x}|\mathbf{y}) \quad (23a)$$

$$\frac{\partial \hat{\Psi}_t(\mathbf{x}|\mathbf{y})}{\partial t} = -\nabla_{\mathbf{x}} \cdot (\hat{\Psi}\mathbf{f})(\mathbf{x}|\mathbf{y}) + \beta_t \frac{1}{2} \Delta \hat{\Psi}_t(\mathbf{x}|\mathbf{y}) \quad (23b)$$

$$s.t. \quad \Psi_0(\mathbf{x}, \mathbf{y}) \hat{\Psi}_0(\mathbf{x}, \mathbf{y}) = p_{\text{join}} \quad \Psi_T(\mathbf{x}, \mathbf{y}) \hat{\Psi}_T(\mathbf{x}, \mathbf{y}) = p_{\text{jprior}} \quad (23c)$$

The solution of (21) is a path measure associated with either the forward (24a), or the backward (24b) SDE with gradients of potentials introduced in (23) added as nonlinear drift terms

$$\begin{cases} d\mathbf{x}_t = [\mathbf{f}_t + \beta_t \nabla_{\mathbf{x}_t} \log \Psi(\mathbf{x}_t, t|\mathbf{y})] dt + \sqrt{\beta_t}d\mathbf{w}_t \\ d\mathbf{y}_t = 0 \\ (\mathbf{x}_0, \mathbf{y}_0) \sim p_{\text{join}} \end{cases} \quad (24a)$$

$$\begin{cases} d\mathbf{x}_t = [\mathbf{f}_t - \beta_t \nabla_{\mathbf{x}_t} \log \hat{\Psi}(\mathbf{x}_t, t|\mathbf{y})] dt + \sqrt{\beta_t}d\bar{\mathbf{w}}_t \\ d\mathbf{y}_t = 0 \\ (\mathbf{x}_T, \mathbf{y}_T) \sim p_{\text{jprior}} \end{cases} \quad (24b)$$

Let $\mathbf{x}_0 \sim p_{\text{data}}$ be the selected element of the training set. If $p_{\text{data}} = \delta_{\mathbf{x}_0}(\cdot)$, then $p_{\text{obs}}(\mathbf{y}) = g(\mathbf{y}|\mathbf{x}_0)$ and $p_{\text{join}}^{\mathbf{x}_0}(\mathbf{x}, \mathbf{y}) = \delta_{\mathbf{x}_0}(\mathbf{x})g(\mathbf{y}|\mathbf{x}_0)$. Consider the joint prior p_{jprior} given by $p_{\text{jprior}}^{\mathbf{x}_0}(\mathbf{x}, \mathbf{y}) = p_{\text{dist}}(\mathbf{x}|\mathbf{x}_0)g(\mathbf{y}|\mathbf{x}_0)$. Similarly to vanilla I²SB, we will approximate the scores of the aggregated set of distribution pairs $(p_{\text{join}}^{\mathbf{x}_0}, p_{\text{jprior}}^{\mathbf{x}_0})$ within the scope of the same deep learning model. To do so, we line for line apply the derivation process of image-to-image Schrödinger Bridge to the system (24). After adapting the notation towards the acoustic inversion problem statement, we arrive at algorithm 1. It solves a particular case of conditional half-bridge problem for general amortized conditional SB statement (13), in which \mathbf{c}_1 continuously drifts towards \mathbf{c}_0 while \mathbf{d}_{obs} remains unchanged throughout the process.

Algorithm 1 Conditional I²SB training

Require: $\mathbf{c}_\theta(\mathbf{c}_t, t, \mathbf{d}_{\text{obs}})$ - denoising neural network, β_t - noise schedule for eq. (9) with $f := 0$, $p_{\text{join}}(\mathbf{c}_0, \mathbf{d}_{\text{obs}})$ - training dataset, $p_{\text{dist}}(\mathbf{c}_1|\mathbf{c}_0)$ - distortion operator, p_{uncond} - probability of unconditional training

- 1: **repeat**
 - 2: Sample $t \sim \mathcal{U}([0, 1])$, $(\mathbf{c}_0, \mathbf{d}_{\text{obs}}) \sim p_{\text{data}}(\mathbf{c}_0, \mathbf{d}_{\text{obs}})$, $\mathbf{c}_1 \sim p_{\text{dist}}(\mathbf{c}_1|\mathbf{c}_0)$
 - 3: Sample $\mathbf{c}_t \sim q(\mathbf{c}_t|\mathbf{c}_0, \mathbf{c}_1)$ according to (17)
 - 4: Take gradient step on θ w.r.t $\|\mathbf{c}_0 - \mathbf{c}_\theta(\mathbf{c}_t, t, \mathbf{d}_{\text{obs}})\|_2^2$
 - 5: **until** converges
-

Excluding observed data \mathbf{d}_{obs} from neural network inputs in alg. 1 results in the exact I²SB training procedure proposed in [25]. Thus, it is possible to learn both conditional and unconditional nonlinear drifts with the same model (alg. 2). During our experiments we have discovered that assigning higher weights for loss terms that include conditional input is beneficial for overall model performance. This behaviour is connected to the prior being informative enough to derive \mathbf{c}_0 purely from \mathbf{c}_1 . Hence, joint cI²SB training procedure without additional weighting tends to converge towards the local minimum in which neural network ignores the conditional input altogether.

Algorithm 2 Guided Conditional I²SB training

Require: $\mathbf{c}_\theta(\mathbf{c}_t, t, \mathbf{d}_{\text{obs}})$ - denoising neural network, β_t - noise schedule for eq. (9) with $f := 0$, $p_{\text{join}}(\mathbf{c}_0, \mathbf{d}_{\text{obs}})$ - training dataset, $p_{\text{dist}}(\mathbf{c}_1|\mathbf{c}_0)$ - distortion operator, p_{uncond} - probability of unconditional training, w_{cond} - loss weighting coefficient in conditional setting

- 1: **repeat**
 - 2: Sample $t \sim \mathcal{U}([0, 1])$, $(\mathbf{c}_0, \mathbf{d}_{\text{obs}}) \sim p_{\text{data}}(\mathbf{c}_0, \mathbf{d}_{\text{obs}})$, $\mathbf{c}_1 \sim p_{\text{dist}}(\mathbf{c}_1|\mathbf{c}_0)$
 - 3: Sample $\mathbf{c}_t \sim q(\mathbf{c}_t|\mathbf{c}_0, \mathbf{c}_1)$ according to (17)
 - 4: Sample $\xi \sim \text{Bin}(p_{\text{uncond}})$.
 - 5: If $\xi = 1$, set $w = 0$, $\mathbf{d}_{\text{obs}} = \mathbf{0}$, else set $w = w_{\text{cond}}$
 - 6: Take gradient step on θ w.r.t $(1 + w) \cdot \|\mathbf{c}_0 - \mathbf{c}_\theta(\mathbf{c}_t, t, \mathbf{d}_{\text{obs}})\|_2^2$
 - 7: **until** converges
-

Following the analogy with classifier-free guidance, we propose a modification to I²SB sampling scheme which employs weighted combination of conditional and unconditional predictions (alg. 3). Intuitively such scheme should reproduce the effect of low-temperature sampling for GANs [37], as similar property was observed in SGM setting [19], although we leave rigorous theoretical treatment of the issue for future studies.

Algorithm 3 Guided Conditional I²SB sampling

- 1: **Input** \mathbf{c}_θ - pretrained denoising neural network, $\mathbf{c}_{\text{smooth}}$ - smoothed velocity model, $\{t_n\}_{n=1}^N$ - time interval discretization, η - guidance scale, \mathbf{d}_{obs} - observed seismic data
 - 2: $\mathbf{c}_N \leftarrow \mathbf{c}_{\text{smooth}}$
 - 3: **for** $n = N$ **to** $n = 1$ **do**
 - 4: Predict $\tilde{\mathbf{c}}_0 = \eta \cdot \mathbf{c}_\theta(\mathbf{c}_n, t_n, \mathbf{d}_{\text{obs}}) + (1 - \eta) \cdot \mathbf{c}_\theta(\mathbf{c}_n, t_n, \mathbf{0})$
 - 5: Sample $\mathbf{c}_{n-1} \sim p(\mathbf{c}_{n-1}|\tilde{\mathbf{c}}_0, \mathbf{c}_n)$ using DDPM posterior
 - 6: **end for**
 - 7: **return** \mathbf{c}_0
-

4 Related works

Wang et al. [21] proposed incorporating diffusion-based regularization into the workflow of acoustic FWI by complementing each denoising step of pre-trained diffusion model with a few iterations of gradient optimization. As a result, the authors claim a level of sample fidelity unattainable with conventional FWI, as well as measurement consistency.

Wang et al. [22] demonstrated that the output of a diffusion model trained on synthetic acoustic velocity fields from the OpenFWI data collection could be manipulated by conditioning on different types of information that might be available during seismic studies. For this purpose, a conditional diffusion model was trained using classifier-free diffusion guidance. The authors report high degree of perceptual similarity to intended velocity fields on validation samples, along with inconsequential deterioration of reconstruction quality on out-of-distribution data.

The paper [23] showcases an alternative way of including multimodal prior information obtained with seismic studies into the DDPM sampling scheme. Namely, Zhang et al. utilize an ensemble of conditional diffusion models to obtain multiple predictions of the original velocity model at each denoising step. Each model works with an individual mode of the available data. A linear combination of predictions with a weighting schedule is employed to proceed to the next step. Reconstruction quality is evaluated on several datasets from the OpenFWI collection, demonstrating superior performance compared to InversionNet and VelocityGAN frameworks [10], [12]. Since the latter were trained with waveform data exclusively, the research indicates that auxiliary information could indeed improve data-driven inversion procedures.

A key limitation of sampling schemes introduced above is their reliance on the standard Gaussian distribution as the terminal diffusion point, despite its lack of connection with the data available to the model at inference stage. Thus, the forward noising process has to run for a sufficiently long time to transfer data points from the original distribution to the standard Gaussian noise. Additionally, the numerical approximation of SDE (4) is only accurate when the discretization timestep is small. This property puts a lower bound on the amount of NFEs required for cSGMs-based inference to perform well. On the other hand, generative models built on the basis of Schrödinger bridges rely neither on limit property of specific class of noising diffusions, nor on the tractability of the prior distribution [35]. These features are critical for us, since they: 1) allow us to construct a theoretically sound foundation for including smoothed velocity fields into diffusion-based acoustic model building; 2) reduce the total computational cost of inference, as Schrödinger bridge-based models generally achieve sample fidelity similar to SGM-based models, but with less NFEs.

5 Results

5.1 Experiment Setup

5.1.1 Model

The architecture chosen for cI^2SB numerical experiments is a variation of the attention-augmented U-Net with timestep embedding proposed in [39] (see fig. 2). We introduce two models to investigate the effect of parameter scaling on framework performance: our **ci2sb-seismic-small** and **ci2sb-seismic-large** models are comprised of approx. $9.5 \cdot 10^5$ and $6.3 \cdot 10^7$ parameters, respectively. Model inputs are $B \times C \times H \times W$ tensors; the first channel of each tensor is reserved for noisy samples \mathbf{c}_t at timestep t , while the remaining channels contain conditional information. SB is conditioned on seismic data \mathbf{d}_{data} with each shot being reduced to the shape of \mathbf{c}_t via linear interpolation. To implement classifier-free guidance [19], we occasionally zero-mask conditional inputs with set probability $p_{\text{uncond}} = 0.5$.

Linear drift for equations (15) is set to $f := 0$, whereas the noise schedule β_t is selected to be shrinking at both boundaries ([25], [34], [35]). Time interval is uniformly split into 1000 sampling steps. Similarly to [40] UNet is parameterised to estimate \mathbf{c}_0 at each denoising iteration. However, network preconditioning and objective rescaling proposed in the same paper did not result in performance gain. We experimented with different values of reweighting coefficient; setting $w_{\text{cond}} = 100$ turned out to be a reliable choice that enhances the performance while keeping the training process stable.

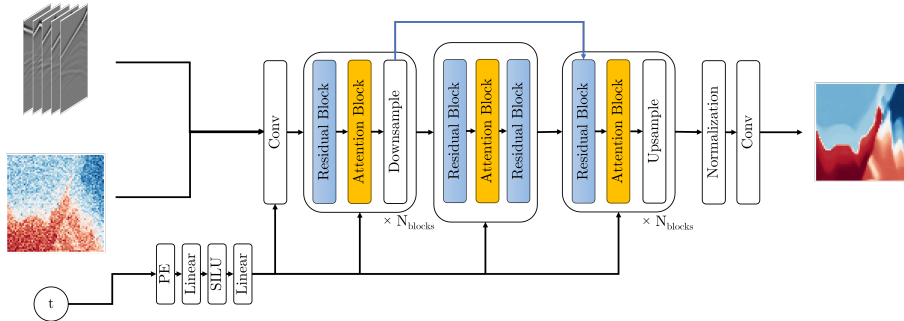


Figure 2: A schematic of attention-augmented UNet network used for numerical studies throughout the study. Original architecture was proposed in [39]

5.1.2 Data

The current study is primarily focused on OpenFWI [26] - an open-access collection of synthetic seismic data. OpenFWI consists of several dataset batches, each corresponding to specific domain of geological interest. Dataset entries are represented by procedurally generated velocity maps and matching waveform data obtained through numerical simulation of acoustic media dynamics (see fig. 3). The closure of the problem statement for numerical modelling is achieved by imposing a free-surface boundary condition on the upper edge and non-reflective boundary condition on the other edges of area under investigation. Modelling is carried out by a finite difference scheme on spatially staggered grid, with order of approximation being second in time and fourth in space. Synthetic waveform data is recorded at a sampling rate of 1000 Hz with equidistant receivers located at the upper edge of the medium. The scanning setup employs 5 source terms scattered over the top boundary of the medium; each emits 15 Hz Ricker wavelet

For training and evaluation purposes we utilize velocity maps and seismic signals from "Vel", "Fault", and "Style" families. Train/validation split ratio for each dataset is kept unchanged from the original paper (tab. 1). Velocity map tensors are resized to the shape $1 \times 64 \times 64$ and scaled to range $[-1, 1]$. In turn, seismograms are subjected to logarithmic transformation, normalized to range $[-1, 1]$, and resized with linear interpolation to be of the shape $5 \times 64 \times 64$.

Group	Dataset	Size	#Train/#Test	Seismic Data Size	Velocity Map Size
Vel Family	FlatVel-A/B	43 GB	24K / 6K	$5 \times 1000 \times 1 \times 70$	$70 \times 1 \times 70$
	CurveVel-A/B	43 GB	24K / 6K	$5 \times 1000 \times 1 \times 70$	$70 \times 1 \times 70$
Fault Family	FlatFault-A/B	77 GB	48K / 6K	$5 \times 1000 \times 1 \times 70$	$70 \times 1 \times 70$
	CurveFault-A/B	77 GB	48K / 6K	$5 \times 1000 \times 1 \times 70$	$70 \times 1 \times 70$
Style Family	Style-A/B	95 GB	60K / 7K	$5 \times 1000 \times 1 \times 70$	$70 \times 1 \times 70$

Table 1: Summary of OpenFWI dataset instances used in the study

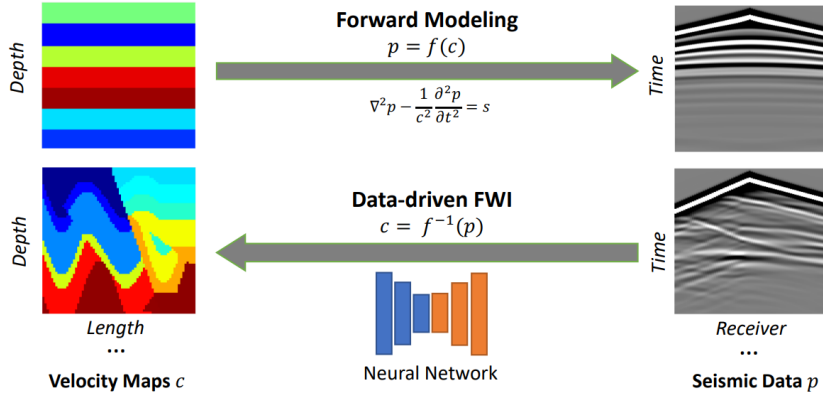


Figure 3: OpenFWI velocity map and seismic data samples [26]

5.1.3 Distortion Operator

The training of cI^2SB assumes the prior distribution at the end of the time interval given by $p(\mathbf{c}_0, \mathbf{c}_1) = p_{\text{data}}(\mathbf{c}_0)p_{\text{dist}}(\mathbf{c}_1|\mathbf{c}_0)$. We provide $p_{\text{dist}}(\cdot|\mathbf{c}_0)$ as a parametric stochastic operator

$$\mathbf{c}_1 = \mathcal{D}_k^\gamma(\mathbf{c}_0) = \mathcal{S}_k(\gamma \cdot \mathbf{z} + (1 - \gamma) \cdot \mathbf{c}_0), \quad \mathbf{z} \sim \mathcal{N}(\mathbf{0}, \mathbf{I}) \quad (25)$$

Here \mathcal{S}_k is the spatial Gaussian filter with kernel size $k \times k$. We set k to be in the integer range from 8 to 16, while γ varies uniformly from 0.0 to 0.2. The design choice for \mathcal{D}_k^γ complies with the concept that initial guesses lack fine-grained details present in the original velocity models. It also ensures high variance of endpoint distributions (fig. 4). Note, however, that suggested construction is generic and does not have any basis in real-world data.

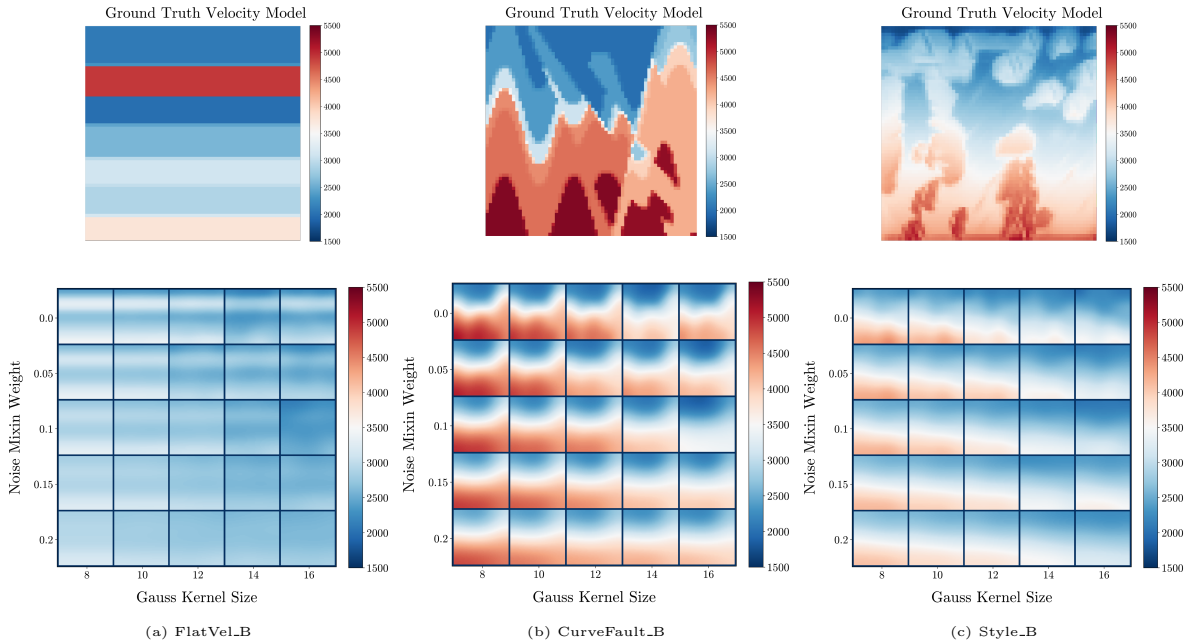


Figure 4: Initial guess distributions obtained via application of degradation operator to velocity model samples from different datasets

5.1.4 Baselines

We contrast the suggested method with our reimplementations of two data-driven seismic inversion frameworks; namely, InversionNet [10], which accepts both seismic data and smoothed velocity models as inputs, as well as the conditional SGM model suggested in [22].

Our implementation of InversionNet is straightforward – we utilize the same network architecture and data processing pipeline proposed in Sections 5.1.1 and 5.1.2, yet pass a constant timestep value for each network call. Given \mathbf{d}_{obs} and \mathbf{c}_1 , InversionNet predicts $\tilde{\mathbf{c}}_0$, which is regressed towards reference velocity distribution \mathbf{c}_0 with MSE loss during training stage.

Our cSGM implementation largely follows the "Improved Denoising Diffusion Probabilistic Models" article [41]. We employ the 1000 step cosine noise schedule proposed in the original paper, but opt out of learning output variance, exclusively estimating \mathbf{c}_0 at each denoising iteration. Conditional inputs for SGM are both seismic data \mathbf{d}_{obs} and smoothed velocity models \mathbf{c}_1 , concatenated along channel axis. Consequently, the neural network architecture used in 5.1.1 is altered to include additional input channel.

5.1.5 Evaluation

For the pivotal experiment, we fit deep learning models on a single data piece obtained by merging dataset entries described in Table 1. As proposed in [26], we utilize validation data to assess inversion quality by measuring the values of MAE, MSE, and SSIM metrics between reconstructed and ground truth velocity models separately for all dataset instances included in the validation subset. Our experiments suggest that diffusion-based algorithms achieve the best possible values for regression metrics with deterministic sampling schemes; specifically, our cSGM implementation uses DDIM sampling with $\sigma_t = 0$ proposed in [42], while I²SB replaces posteriors with their means during inference. By default, it is assumed that sampling procedures for cSGM and cI²SB utilize 50 network calls each; i.e, the NFE parameter is set to 50. A more detailed study on the impact of such parameter on inversion quality could be found in section 6.

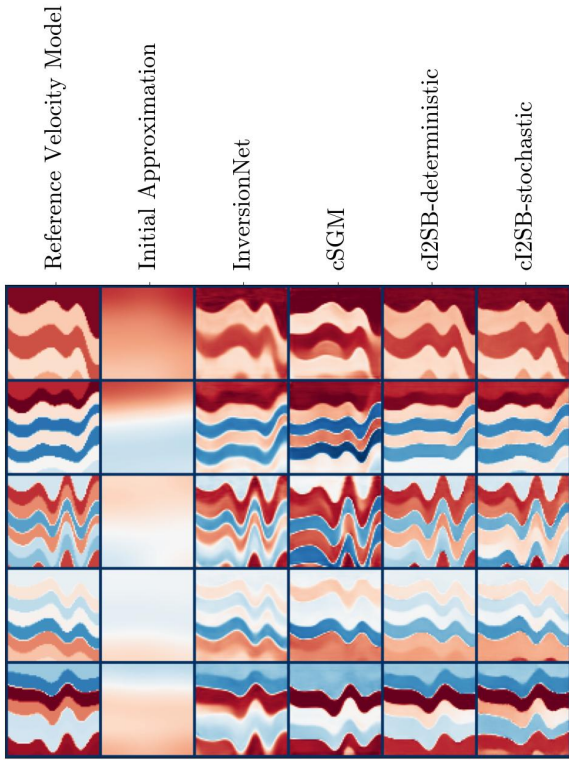
5.2 Experiment Results

Tables 2 and 3 provide a performance assessment of **ci2sb-seismic-small** and **ci2sb-seismic-large** model instances trained as cI²SB compared to counterpart frameworks. For completeness, we also provide results of stochastic sampling with the cI²SB model while averaging the metrics values over 50 different random seeds. Figures 5 and 6 showcases difference between inversion procedures applied to a batch of data from validation subsets of CurveVel-B, FlatFault-B, CurveFault-B and Style-B datasets. Figure 7 displays instances of stochastic cI²SB sampling trajectories. The following takeaways summarize the observed data:

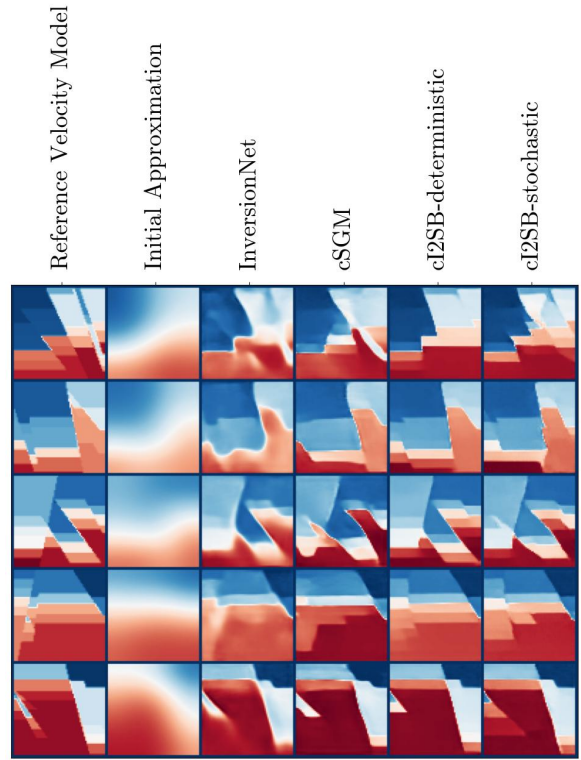
- Our reimplement of InversionNet is a valid reference point, surpassing the performance of state-of-the-art solution [46] provided the additional information given by smooth velocity models.
- The **ci2sb-seismic-small** model instance trained in a purely supervised fashion on average performs better than both cSGM and cI²SB with respect to the selected evaluation criteria. However, our reimplement of InversionNet is incapable of reproducing fine details observed on velocity fields reconstructed with diffusion-based frameworks.
- Parameter scaling favours the proposed method, as **ci2sb-seismic-large** model instance trained as conditional I²SB reduces the performance gap observed earlier, while maintaining texture quality that better aligns with human perception. Furthermore, stochastic sampling scheme for cI²SB was able to reproduce texture-level velocity field variations characteristic of Style-B dataset. Concerning the studies that utilize OpenFWI for model performance evaluation, this result, to our knowledge, is novel.
- In all studied cases training scheme based on cI²SB outperforms the one based on cSGM by statistically significant margin.

Table 2: Survey of **ci2sb-seismic-small** model performance within the scope of different data-driven seismic inversion frameworks.

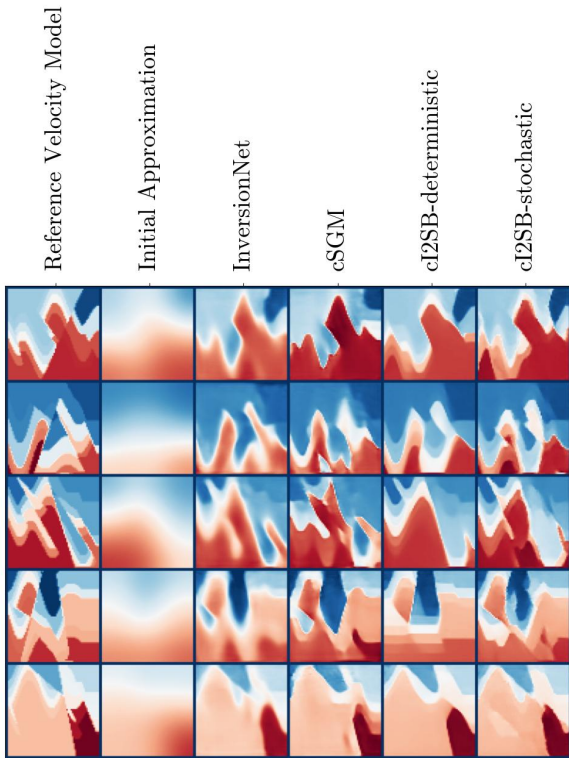
	InversionNet			cSGM			OT-ODE sampling with cI ² SB			Stochastic sampling with cI ² SB		
	MAE ↓	MSE ↓	SSIM ↑	MAE ↓	MSE ↓	SSIM ↑	MAE ↓	MSE ↓	SSIM ↑	MAE ↓	MSE ↓	SSIM ↑
FlatVel_A	1.78e-3	8.36e-4	0.9782	3.96e-2	4.06e-3	0.9442	2.07e-2	1.25e-3	0.9826	3.43e-2	3.69e-3	0.9564
FlatVel_B	3.57e-2	4.26e-3	0.9484	9.27e-2	2.55e-2	0.8419	5.24e-2	1.25e-2	0.9150	7.23e-2	2.04e-2	0.8731
CurveVel_A	3.66e-2	3.79e-3	0.9224	6.23e-2	1.11e-2	0.8529	4.31e-2	5.89e-3	0.9227	6.29e-2	1.25e-2	0.8708
CurveVel_B	7.47e-2	1.75e-3	0.8597	1.36e-1	5.48e-2	0.7184	9.71e-2	3.30e-2	0.8102	1.20e-1	4.77e-2	0.7563
FlatFault_A	1.72e-2	1.01e-3	0.9825	3.99e-2	4.90e-3	0.9613	2.07e-2	1.44e-3	0.9839	2.94e-2	3.24e-3	0.9701
FlatFault_B	5.68e-2	8.69e-3	0.8586	1.01e-1	2.67e-2	0.7469	7.37e-2	1.55e-2	0.8240	9.44e-2	2.42e-2	0.7611
CurveFault_A	2.37e-2	2.07e-3	0.9681	4.38e-2	7.18e-3	0.9333	3.01e-2	3.37e-3	0.9666	4.04e-2	6.35e-3	0.9439
CurveFault_B	8.86e-2	1.89e-3	0.7778	1.42e-1	4.73e-2	0.6300	1.21e-1	3.40e-2	0.7083	1.44e-1	4.97e-2	0.6336
Style_A	3.80e-2	3.27e-3	0.9370	6.74e-2	1.01e-2	0.8562	5.10e-2	5.91e-3	0.9100	7.40e-2	1.25e-2	0.8531
Style_B	5.17e-2	5.34e-3	0.8011	8.00e-2	1.34e-2	0.6733	5.89e-2	7.81e-3	0.7748	7.74e-2	1.30e-2	0.6853



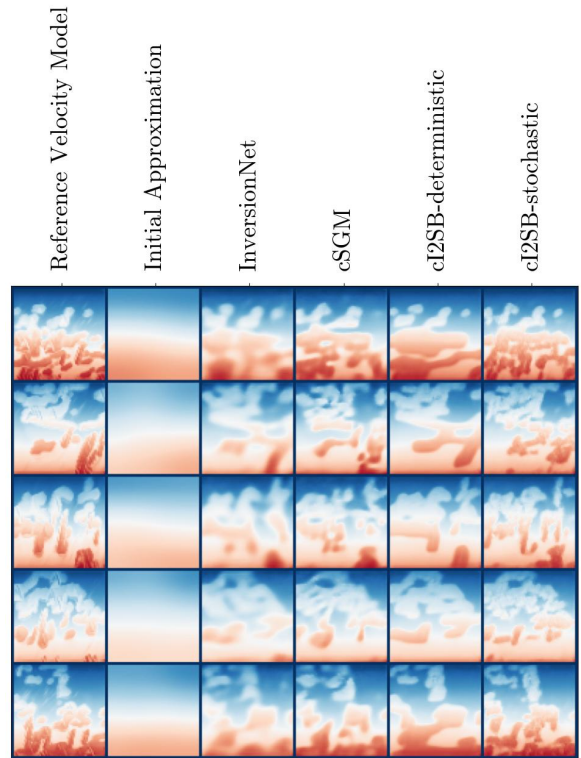
(a) CurveVel_B



(b) FlatFault_B

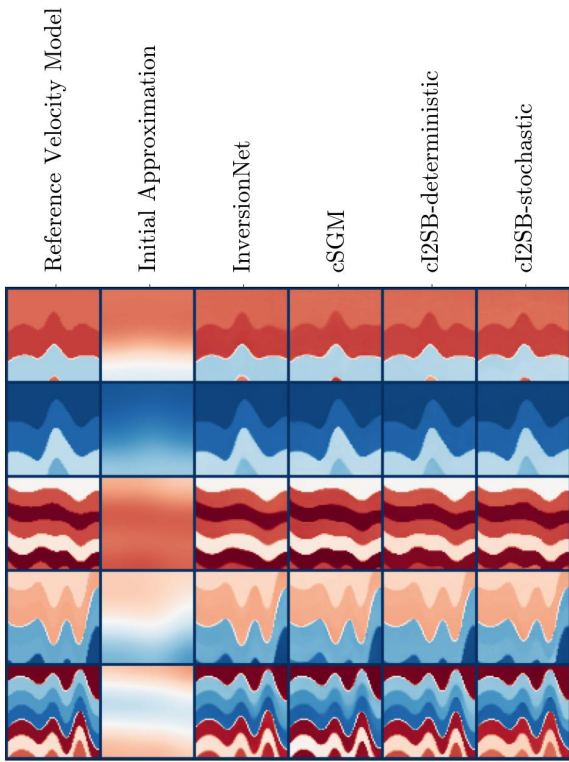


(c) CurveFault_B

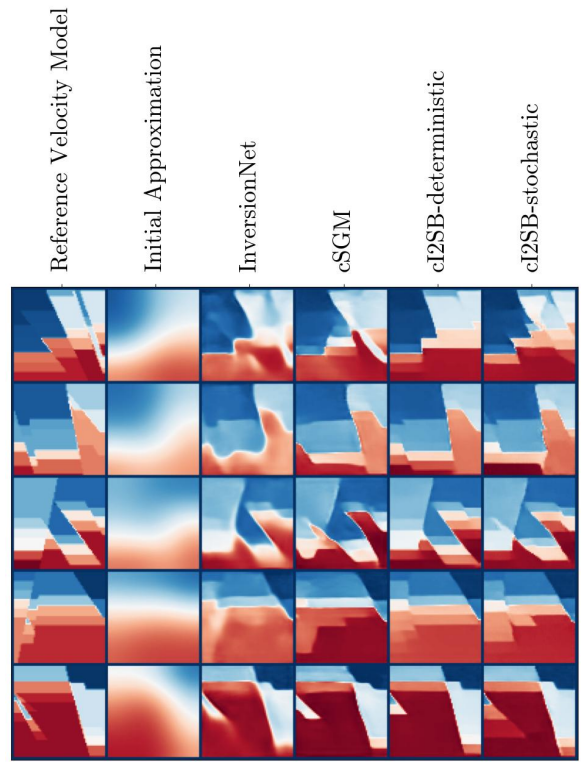


(d) Style_B

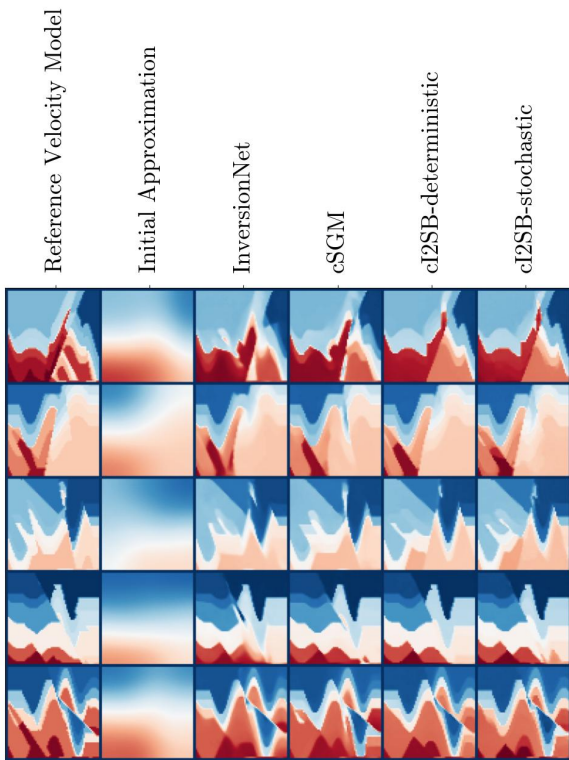
Figure 5: Velocity models obtained through deep-learning based seismic inversion in comparison with ground truth velocity models. The backbone neural network is `ci2sb-seismic-small`.



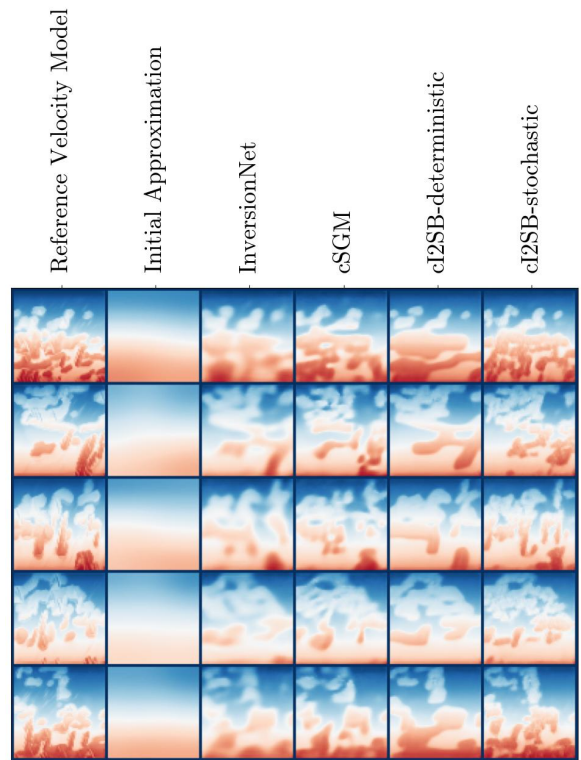
(a) CurveVel_B



(b) FlatFault_B



(c) CurveFault_B



(d) Style_B

Figure 6: Velocity models obtained through deep-learning based seismic inversion in comparison with ground truth velocity models. The backbone neural network is **cI2sb-seismic-large**.

Table 3: Survey of **ci2sb-seismic-large** model performance within the scope of different data-driven seismic inversion frameworks.

	InversionNet			cSGM			OT-ODE sampling with ci^2SB			Stochastic sampling with ci^2SB		
	MAE ↓	MSE ↓	SSIM ↑	MAE ↓	MSE ↓	SSIM ↑	MAE ↓	MSE ↓	SSIM ↑	MAE ↓	MSE ↓	SSIM ↑
FlatVel_A	3.87e-3	4.19e-5	0.9990	6.57e-3	1.11e-4	0.9961	6.62e-3	1.56e-4	0.9991	6.75e-3	1.57e-4	0.9977
FlatVel_B	1.03e-3	8.06e-4	0.9916	2.01e-2	2.31e-3	0.9787	1.72e-2	3.01e-3	0.9796	2.07e-2	3.65e-3	0.9745
CurveVel_A	1.26e-2	9.53e-4	0.9803	1.61e-2	1.46e-3	0.9713	1.25e-2	1.04e-3	0.9825	1.60e-2	1.48e-3	0.9752
CurveVel_B	3.40e-2	7.56e-3	0.9475	4.26e-2	1.01e-2	0.9320	3.50e-2	9.21e-3	0.9420	4.16e-2	1.20e-2	0.9269
FlatFault_A	5.38e-3	1.39e-4	0.9968	8.05e-3	3.03e-4	0.9933	6.62e-3	1.56e-4	0.9973	8.62e-3	2.48e-3	0.9955
FlatFault_B	2.76e-2	3.96e-3	0.9356	3.29e-2	5.42e-3	0.9154	2.53e-2	3.70e-3	0.9467	3.14e-2	4.85e-3	0.9321
CurveFault_A	7.76e-3	3.64e-4	0.9932	1.07e-2	6.72e-4	0.9898	8.86e-3	3.58e-4	0.9944	1.13e-2	5.48e-3	0.9913
CurveFault_B	6.48e-2	1.41e-2	0.8343	7.07e-2	1.74e-2	0.8121	6.06e-2	1.36e-2	0.8542	7.06e-2	1.72e-2	0.8241
Style_A	2.28e-2	1.52e-3	0.9681	2.91e-2	2.35e-3	0.9537	2.61e-2	2.04e-3	0.9672	3.50e-2	3.60e-3	0.9480
Style_B	3.41e-2	2.86e-3	0.8832	4.35e-2	4.93e-3	0.8260	3.35e-2	3.18e-3	0.8904	4.24e-2	4.83e-3	0.8477

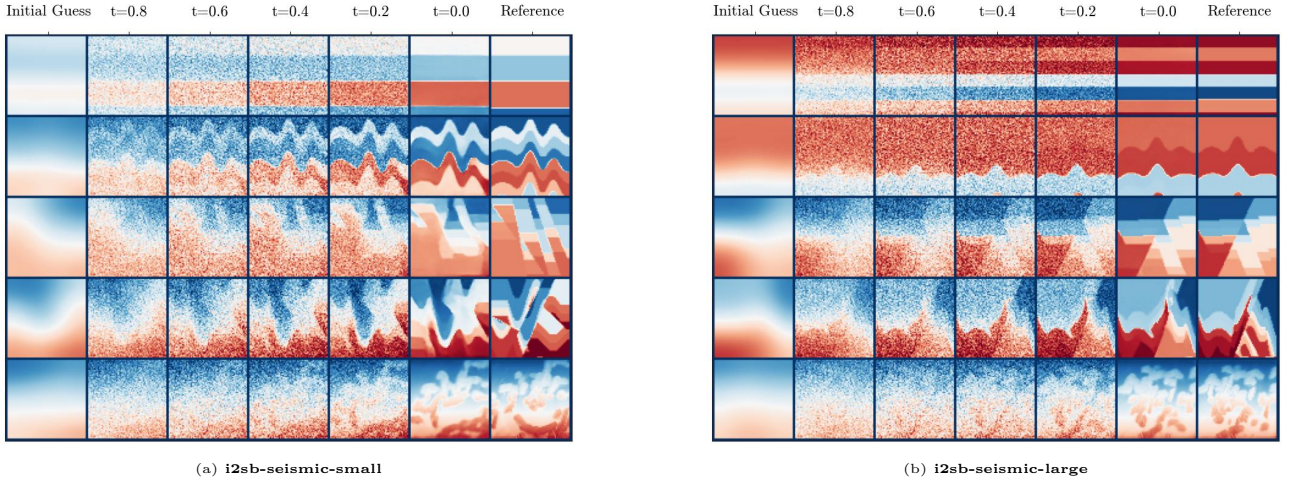


Figure 7: Generative process of ci^2SB for model instances trained on the entirety of the OpenFWI collection.

6 Discussion

6.1 Objective reweighting

The use of sampling scheme 3 for **ci2sb-seismic-small** model instance trained with alg. 2 while w_{cond} is set 0 leads to the inferior performance compared to both InversionNet, cSGM, and the same model instance trained with alg. 1. However, applying baseline classifier-free guidance to cSGM does not affect its performance in the same way, as the decay in values of quality metrics for such framework is less significant (fig. 8). Therefore, we believe that the reasoning for performance drop lies in prior distribution at terminal diffusion point shifting from pure gaussian to the mixture of the ones induced with degradation operator.

To rationalize the observed phenomenon, we revisit the joint ci^2SB training scheme. At each step neural network is asked to reconstruct the initial point \mathbf{c}_0 of diffusion bridge given either noisy sample \mathbf{c}_t , or \mathbf{c}_t combined with conditional input \mathbf{d}_{obs} . By model design, \mathbf{c}_t is close to \mathbf{c}_0 , meanwhile the mapping between \mathbf{d}_{obs} and \mathbf{c}_0 might be arbitrarily complex. As the target variable for score matching is independent of \mathbf{d}_{obs} , the natural course of action for neural network when $w_{\text{cond}} = 0$ is to *pay less attention to the conditional input*, inferring the regression target mostly from \mathbf{c}_t . Indeed, in the case above the gap between evaluation metrics calculated with velocity models obtained through conditional and unconditional sampling is minor. However, as seen in fig. 8, explicitly nudging joint ci^2SB training procedure towards conditional evaluation via objective reweighting solves the issues, bringing model’s performance in line with other solutions at the cost of the quality of unconditional evaluation.

6.2 Sample fidelity and regression metrics

The number of NFEs required to obtain samples with high image fidelity represents a critical hyperparameter in diffusion-based inference, determining its total computational cost. Since better performance at low NFE regimes is the desired property of such algorithms, we study impact of utilizing more NFEs for conditional stochastic I^2SB sampling on the value of regression metrics proposed for model evaluation. Results of our findings for the **ci2sb-seismic-large** model instance described in 5.1.1 are presented with tables 4 and 5.

Figure 9 depicts batches from validation subsets of CurveVel_B, FlatFault_B, CurveFault_B, and Style_B datasets respectively, along with reconstructed data obtained through ci^2SB sampling procedure in different NFE regimes. For illustrative purposes we extend the range for NFEs up to 1000. As the evidence shows, despite the noticeable difference in perceptual quality, utilizing more NFEs per inference run does not necessarily lead

Table 4: The dependency of validation metrics estimated cI^2SB from the amount of NFEs, part 1

	NFE=1			NFE=2			NFE=5		
	MAE ↓	MSE ↓	SSIM ↑	MAE ↓	MSE ↓	SSIM ↑	MAE ↓	MSE ↓	SSIM ↑
FlatVel_A	4.22e-3	4.24e-5	0.9989	4.35e-3	4.74e-5	0.9991	4.74e-3	6.02e-5	0.9991
FlatVel_B	1.63e-2	1.71e-2	0.9841	1.46e-2	1.84e-2	0.9845	1.54e-2	1.99e-3	0.9836
CurveVel_A	1.36e-2	9.90e-4	0.9807	1.38e-2	1.06e-4	0.9806	1.47e-2	1.26e-3	0.9783
CurveVel_B	3.87e-2	8.32e-3	0.9432	3.64e-2	8.99e-3	0.9427	3.81e-2	1.02e-3	0.9364
FlatFault_A	5.49e-3	1.28e-4	0.9969	5.93e-3	1.39e-4	0.9970	6.60e-3	1.71e-4	0.9973
FlatFault_B	2.75e-2	3.57e-3	0.9429	2.82e-2	3.90e-3	0.9406	3.06e-2	4.62e-3	0.9326
CurveFault_A	7.84e-3	3.35e-4	0.9935	8.35e-3	3.55e-4	0.9937	9.38e-3	4.34e-4	0.9930
CurveFault_B	6.36e-2	1.30e-2	0.8507	6.40e-2	1.37e-2	0.8472	6.84e-2	1.57e-2	0.8321
Style_A	2.62e-2	2.01e-3	0.9643	2.83e-2	2.33e-3	0.9608	3.20e-2	3.01e-3	0.9534
Style_B	3.55e-2	3.04e-3	0.8813	3.72e-2	3.50e-3	0.8726	4.03e-2	4.29e-3	0.8564

Table 5: The dependency of validation metrics estimated with cI^2SB from the amount of NFEs, part 2

	NFE=10			NFE=20			NFE=50		
	MAE ↓	MSE ↓	SSIM ↑	MAE ↓	MSE ↓	SSIM ↑	MAE ↓	MSE ↓	SSIM ↑
FlatVel_A	5.04e-3	6.80e-5	0.9989	5.42e-3	7.71e-5	0.9986	5.86e-3	8.28e-5	0.9981
FlatVel_B	1.61e-2	2.08e-3	0.9826	1.69e-2	2.19e-3	0.9817	1.76e-2	2.37e-3	0.9807
CurveVel_A	1.54e-2	1.40e-3	0.9765	1.59e-2	1.48e-3	0.9751	1.66e-2	1.57e-3	0.9732
CurveVel_B	3.97e-2	1.10e-2	0.9317	4.09e-2	1.16e-2	0.9286	4.32e-2	1.21e-2	0.9255
FlatFault_A	7.04e-3	1.90e-4	0.9965	7.49e-3	2.11e-4	0.9962	8.08e-3	2.33e-4	0.9954
FlatFault_B	3.24e-2	5.08e-3	0.9278	3.37e-2	5.42e-3	0.9238	3.46e-2	5.64e-3	0.9210
CurveFault_A	9.92e-3	4.76e-4	0.9925	1.04e-2	5.15e-4	0.9919	1.10e-2	5.53e-4	0.9909
CurveFault_B	7.16e-2	1.71e-2	0.8219	7.41e-2	1.83e-2	0.8137	7.63e-2	1.93e-2	0.8068
Style_A	3.44e-2	3.50e-3	0.9480	3.61e-2	3.86e-3	0.9440	3.77e-2	4.16e-3	0.9403
Style_B	4.29e-2	4.79e-3	0.8457	4.40e-2	5.17e-3	0.8371	4.59e-2	5.57e-3	0.8271

to higher value of suggested evaluation metrics. On the contrary, the average value of MAE and MSE on the validation set increases with additional neural network calls, whereas SSIM steadily decreases. This observation aligns with the perception-distortion tradeoff [47] – the characteristic previously observed in various generative modelling frameworks, including bridge-like models [48].

We believe that perception-distortion tradeoff achieved with cI^2SB inference could be credited to bias amplification in sampling scheme, as velocity model estimates through denoising timesteps utilize neural network with the shared set of parameters. Figure 10 illustrates the phenomenon through vertical slices of velocity models presented in Figure 9 at fixed grid nodes, revealing that consecutive I^2SB iterations can significantly shift velocity profiles of predicted \mathbf{c}_0 away from ground truth. In comparison, one-step estimates of \mathbf{c}_0 with the same network given the timestep t and the intermediate point \mathbf{c}_t sampled with (17) are increasingly more accurate at the beginning of bridge (fig. 11). Further research could be directed towards mitigating such issue, however, it is out of the scope of the current study.

In addition, we present empirical evidence to support the claim that Schrödinger Bridge-based models achieve high perceptual quality of samples with fewer NFEs compared to SGM-based models. Namely, we illustrate several batches of reconstructed velocity fields from validation subset with NFEs ranging from 1 to 1000 (fig 12). The difference in perceptual quality is most noticeable for samples from Style-B subset, since in this case inference process for cSGM is unable to capture the texture-level details until NFE parameter is set to 100 or higher. In comparison, high-frequency detailing of velocity fields reconstructed with cI^2SB is observable starting from NFE=5.

6.3 Classifier-free Guidance in application to cI^2SB

Our experiments demonstrate that inference procedure 3 for cI^2SB model trained with algorithm 2 provides an additional degree of control over the variance of output samples through the guidance scale parameter η . To demonstrate that, we display velocity models recovered from distribution of initial guesses obtained through p_{prior} with the same reference velocity model depending on value of η (fig. 13).

The diversity in reconstructed velocity models shows an inverse correlation with η values - for instance, setting $\eta = 0.2$ results in more diverse output compared to $\eta = 0.8$. As the value of guidance scale approaches $\eta = 1$, i.e., for purely conditional inference, modes of output distributions "collapse", resulting in nearly constant reconstruction outcome regardless of initial guess. At the same time, with η set to 0, which is equivalent to I^2SB sampling, model output exhibits the most significant degree of variance. Hence, we substantiate our claim about guidance scale acting as an equivalent of inverse temperature for GAN output manipulation.

6.4 Limitations

From the perspective of data-related issues, the major open challenges in the field of deep learning-based FWI are the inherent noise in seismic data and transferability of models between different basins of geological structures and acquisition geometries [6]. The first issue can be partially addressed with the suggested framework, since the joint prior distribution can be selected with noisy observations and smoothed velocity models in mind. However, the implementation of classifier-free guidance relies on the constant shape of the conditioning vector, thus, only exacerbating the second issue, as the representation of seismograms greatly varies depending on acquisition setup.

Another limiting factor of the developed framework is its reliance on the explicit design of distortion operator \mathcal{D}_k^γ . Hence, the quality of inversion is subject to degradation if inference distribution of initial guesses differs from the one used for model training. To illustrate the case, we repeat the cI^2SB evaluation procedure for two different operators $\hat{\mathcal{D}}_k^\gamma$ and $\tilde{\mathcal{D}}_k^\gamma$: for the first one k belongs in the integer range from 16 to 24, whereas for the second one the same parameter varies from 0 to 8 (table 6). The results of the proposed experiment reveal that the inferior value of metrics on the out-of-distribution smooth models is related to the distribution shift per se. Indeed, initial guesses obtained through the second distortion operator are arguably more informative than those used during parameter tuning, yet cI^2SB -based inversion performs better when smooth models align with samples from training distribution. Thus, despite the developed procedure having improved theoretical grounding compared to previous iterations of data-driven algorithms, it still lacks robustness of classical waveform inversion pipelines.

	cI ² SB with initial guesses obtained through $\hat{\mathcal{D}}_k^\gamma$			cI ² SB with initial guesses obtained through $\tilde{\mathcal{D}}_k^\gamma$		
	MAE ↓	MSE ↓	SSIM ↑	MAE ↓	MSE ↓	SSIM ↑
FlatVel.A	2.24e−2	1.84e−3	0.9853	1.12e−2	6.63e−4	0.9952
FlatVel.B	4.91e−2	1.50e−2	0.9265	5.97e−2	1.37e−2	0.9292
CurveVel.A	3.02e−2	3.40e−3	0.9672	2.51e−2	3.50e−3	0.9669
CurveVel.B	6.27e−2	2.07e−3	0.8989	8.85e−2	2.72e−3	0.8855
FlatFault.A	1.92e−2	1.11e−3	0.9932	1.66e−2	8.21e−4	0.9939
FlatFault.B	4.39e−2	7.60e−3	0.9155	3.93e−2	6.91e−3	0.9321
CurveFault.A	2.25e−2	1.53e−3	0.9887	1.94e−2	1.18e−3	0.9899
CurveFault.B	8.65e−2	2.35e−2	0.7984	9.07e−2	2.63e−2	0.8233
Style.A	4.72e−2	6.97e−3	0.9319	3.83e−2	4.27e−3	0.9515
Style.B	4.69e−2	5.62e−3	0.8415	3.95e−2	4.11e−3	0.8638

Table 6: cI²SB inversion results for out-of-distribution initial guesses.

7 Conclusion

We develop a variation to the recently proposed data-driven approach to acoustic waveform inversion with diffusion models. The theoretical backbone of our method is a special case of conditional Schrödinger Bridge problem which admits reformulation that makes the training process tractable. Our method demonstrates significant improvements over the previous results on the subject, achieving comparable performance to supervised-learning methods with only a few NFEs while producing samples that better align with human perceptual quality. Furthermore, the proposed training procedure enables an additional degree of control over output variance through the guidance scale hyperparameter.

References

- [1] B. H. Russell, *Introduction to seismic inversion methods*. SEG Books, 1988.
- [2] G. T. Schuster, *Seismic inversion*. Society of Exploration Geophysicists, 2017.
- [3] J. O. Robertsson, B. Bednar, J. Blanch, C. Kostov, and D.-J. van Manen, *Introduction to the supplement on seismic modeling with applications to acquisition, processing, and interpretation*, 2007.
- [4] R. Alford, K. Kelly, and D. M. Boore, “Accuracy of finite-difference modeling of the acoustic wave equation,” *Geophysics*, vol. 39, no. 6, pp. 834–842, 1974.
- [5] A. Adler, M. Araya-Polo, and T. Poggio, “Deep learning for seismic inverse problems: Toward the acceleration of geophysical analysis workflows,” *IEEE Signal Processing Magazine*, vol. 38, no. 2, pp. 89–119, 2021.
- [6] S. M. Mousavi, G. C. Beroza, T. Mukerji, and M. Rasht-Behesht, “Applications of deep neural networks in exploration seismology: A technical survey,” *Geophysics*, vol. 89, no. 1, WA95–WA115, 2024.
- [7] M. Araya-Polo, J. Jennings, A. Adler, and T. Dahlke, “Deep-learning tomography,” *The Leading Edge*, vol. 37, no. 1, pp. 58–66, 2018.

- [8] W. Zhang, J. Gao, Z. Gao, and H. Chen, “Adjoint-driven deep-learning seismic full-waveform inversion,” *IEEE Transactions on Geoscience and Remote Sensing*, vol. 59, no. 10, pp. 8913–8932, 2020.
- [9] W. Zhang and J. Gao, “Deep-learning full-waveform inversion using seismic migration images,” *IEEE Transactions on Geoscience and Remote Sensing*, vol. 60, pp. 1–18, 2021.
- [10] Y. Wu and Y. Lin, “Inversionnet: An efficient and accurate data-driven full waveform inversion,” *IEEE Transactions on Computational Imaging*, vol. 6, pp. 419–433, 2019.
- [11] F. Yang and J. Ma, “Deep-learning inversion: A next-generation seismic velocity model building method,” *Geophysics*, vol. 84, no. 4, R583–R599, 2019.
- [12] Z. Zhang and Y. Lin, “Data-driven seismic waveform inversion: A study on the robustness and generalization,” *IEEE Transactions on Geoscience and Remote Sensing*, vol. 58, no. 10, pp. 6900–6913, 2020.
- [13] J. Ho, A. Jain, and P. Abbeel, “Denoising diffusion probabilistic models,” *Advances in neural information processing systems*, vol. 33, pp. 6840–6851, 2020.
- [14] L. Yang, Z. Zhang, Y. Song, *et al.*, “Diffusion models: A comprehensive survey of methods and applications,” *ACM Computing Surveys*, vol. 56, no. 4, pp. 1–39, 2023.
- [15] Y. Song, J. Sohl-Dickstein, D. P. Kingma, A. Kumar, S. Ermon, and B. Poole, “Score-based generative modeling through stochastic differential equations,” *arXiv preprint arXiv:2011.13456*, 2020.
- [16] H. Li, Y. Yang, M. Chang, *et al.*, “Srdiff: Single image super-resolution with diffusion probabilistic models,” *Neurocomputing*, vol. 479, pp. 47–59, 2022.
- [17] A. Lugmayr, M. Danelljan, A. Romero, F. Yu, R. Timofte, and L. Van Gool, “Repaint: Inpainting using denoising diffusion probabilistic models,” in *Proceedings of the IEEE/CVF conference on computer vision and pattern recognition*, 2022, pp. 11 461–11 471.
- [18] B. Kawar, M. Elad, S. Ermon, and J. Song, “Denoising diffusion restoration models,” *Advances in Neural Information Processing Systems*, vol. 35, pp. 23 593–23 606, 2022.
- [19] J. Ho and T. Salimans, *Classifier-free diffusion guidance*, 2022. arXiv: 2207.12598 [cs.LG].
- [20] R. Rombach, A. Blattmann, D. Lorenz, P. Esser, and B. Ommer, *High-resolution image synthesis with latent diffusion models*, 2022. arXiv: 2112.10752 [cs.CV].
- [21] F. Wang, X. Huang, and T. A. Alkhalifah, *IEEE Transactions on Geoscience and Remote Sensing*, vol. 61, pp. 1–11, 2023.
- [22] F. Wang, X. Huang, and T. Alkhalifah, “Controllable seismic velocity synthesis using generative diffusion models,” *Journal of Geophysical Research: Machine Learning and Computation*, vol. 1, no. 3, e2024JH000153, 2024.
- [23] H. Zhang, Y. Li, and J. Huang, “Diffusionvel: Multi-information integrated velocity inversion using generative diffusion models,” *arXiv preprint arXiv:2410.21776*, 2024.
- [24] Y. Shi, V. De Bortoli, G. Deligiannidis, and A. Doucet, “Conditional simulation using diffusion schrödinger bridges,” in *Uncertainty in Artificial Intelligence*, PMLR, 2022, pp. 1792–1802.
- [25] G.-H. Liu, A. Vahdat, D.-A. Huang, E. A. Theodorou, W. Nie, and A. Anandkumar, *I²sb: Image-to-image schrödinger bridge*, 2023. arXiv: 2302.05872 [cs.CV].
- [26] C. Deng, Y. Feng, S. Feng, *et al.*, “Openfwi: Benchmark seismic datasets for machine learning-based full waveform inversion,” *CoRR*, vol. abs/2111.02926, 2021. arXiv: 2111.02926.
- [27] “An overview of full-waveform inversion in exploration geophysics,” *Geophysics*, vol. 74, no. 6, WCC1–WCC26, 2009.
- [28] B. D. Anderson, “Reverse-time diffusion equation models,” *Stochastic Processes and their Applications*, vol. 12, no. 3, pp. 313–326, 1982.
- [29] P. Vincent, “A connection between score matching and denoising autoencoders,” *Neural computation*, vol. 23, no. 7, pp. 1661–1674, 2011.
- [30] E. Schrödinger, “Sur la théorie relativiste de l’électron et l’interprétation de la mécanique quantique,” in *Annales de l’institut Henri Poincaré*, vol. 2, 1932, pp. 269–310.
- [31] M. Pavon and A. Wakolbinger, “On free energy, stochastic control, and schrödinger processes,” in *Modeling, Estimation and Control of Systems with Uncertainty: Proceedings of a Conference held in Sopron, Hungary, September 1990*, Springer, 1991, pp. 334–348.
- [32] C. Léonard, “A survey of the schrödinger problem and some of its connections with optimal transport,” *arXiv preprint arXiv:1308.0215*, 2013.

- [33] Y. Chen, T. T. Georgiou, and M. Pavon, “Stochastic control liaisons: Richard sinkhorn meets gaspard monge on a schrodinger bridge,” *Siam Review*, vol. 63, no. 2, pp. 249–313, 2021.
- [34] T. Chen, G.-H. Liu, and E. A. Theodorou, “Likelihood training of schrödinger bridge using forward-backward sdes theory,” *arXiv preprint arXiv:2110.11291*, 2021.
- [35] V. De Bortoli, J. Thornton, J. Heng, and A. Doucet, “Diffusion schrödinger bridge with applications to score-based generative modeling,” *Advances in Neural Information Processing Systems*, vol. 34, pp. 17 695–17 709, 2021.
- [36] Y. Chen, T. T. Georgiou, and M. Pavon, *Stochastic control liaisons: Richard sinkhorn meets gaspard monge on a schrodinger bridge*, 2020. arXiv: 2005.10963 [math.OC].
- [37] A. Brock, J. Donahue, and K. Simonyan, “Large scale gan training for high fidelity natural image synthesis,” *arXiv preprint arXiv:1809.11096*, 2018.
- [38] H. Chung, B. Sim, D. Ryu, and J. C. Ye, *Improving diffusion models for inverse problems using manifold constraints*, 2022. arXiv: 2206.00941 [cs.LG].
- [39] P. Dhariwal and A. Nichol, “Diffusion models beat gans on image synthesis,” *CoRR*, vol. abs/2105.05233, 2021. arXiv: 2105.05233.
- [40] T. Karras, M. Aittala, T. Aila, and S. Laine, *Elucidating the design space of diffusion-based generative models*, 2022. arXiv: 2206.00364 [cs.CV].
- [41] A. Nichol and P. Dhariwal, “Improved denoising diffusion probabilistic models,” *CoRR*, vol. abs/2102.09672, 2021. arXiv: 2102.09672.
- [42] J. Song, C. Meng, and S. Ermon, “Denoising diffusion implicit models,” *arXiv preprint arXiv:2010.02502*, 2020.
- [43] G. O. Roberts and R. L. Tweedie, “Exponential convergence of langevin distributions and their discrete approximations,” *Bernoulli*, pp. 341–363, 1996.
- [44] A. Nguyen, J. Clune, Y. Bengio, A. Dosovitskiy, and J. Yosinski, “Plug & play generative networks: Conditional iterative generation of images in latent space,” in *Proceedings of the IEEE conference on computer vision and pattern recognition*, 2017, pp. 4467–4477.
- [45] H. Chung, J. Kim, M. T. Mccann, M. L. Klasky, and J. C. Ye, “Diffusion posterior sampling for general noisy inverse problems,” *arXiv preprint arXiv:2209.14687*, 2022.
- [46] P. Jin, Y. Feng, S. Feng, *et al.*, “An empirical study of large-scale data-driven full waveform inversion,” *Scientific Reports*, vol. 14, no. 1, p. 20 034, 2024.
- [47] Y. Blau and T. Michaeli, “The perception-distortion tradeoff,” in *Proceedings of the IEEE conference on computer vision and pattern recognition*, 2018, pp. 6228–6237.
- [48] M. Delbraccio and P. Milanfar, “Inversion by direct iteration: An alternative to denoising diffusion for image restoration,” *arXiv preprint arXiv:2303.11435*, 2023.

Supplementary figures

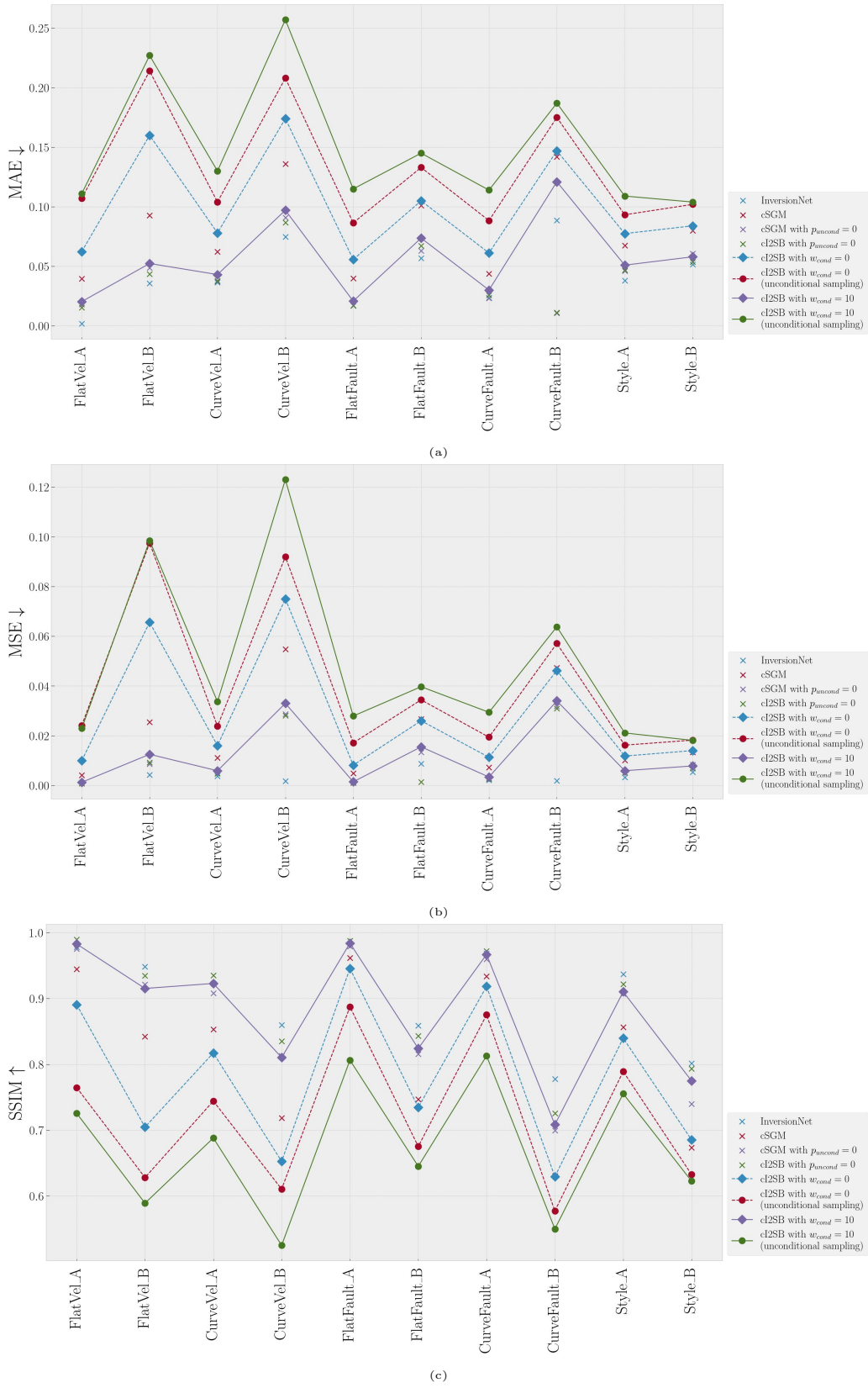
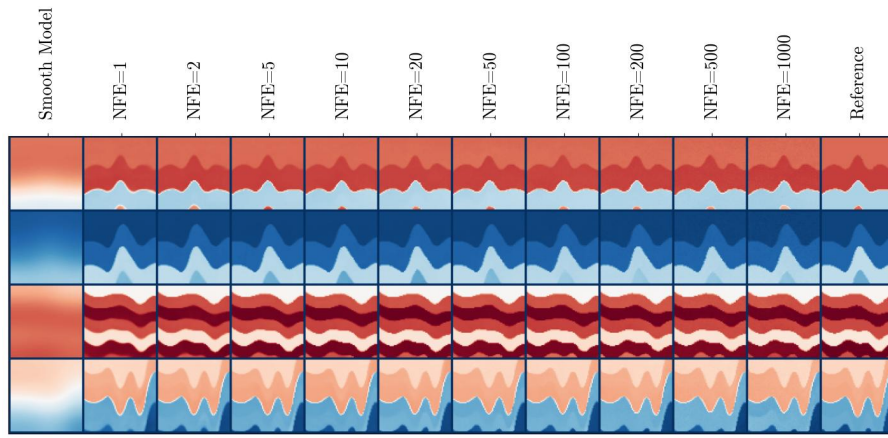
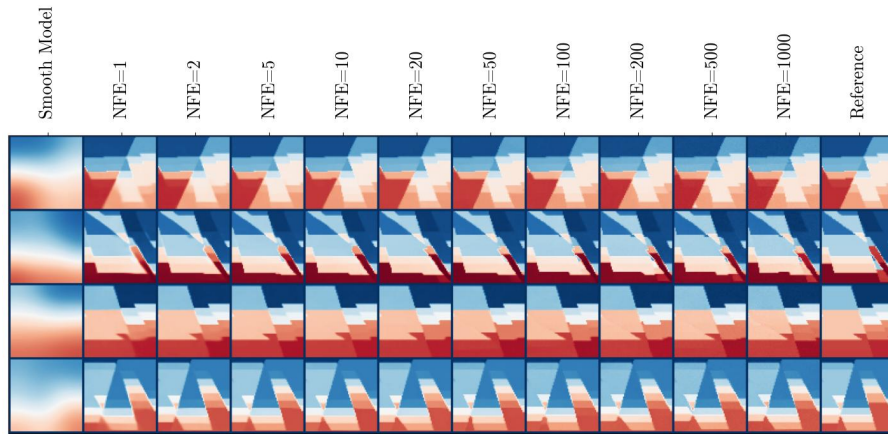


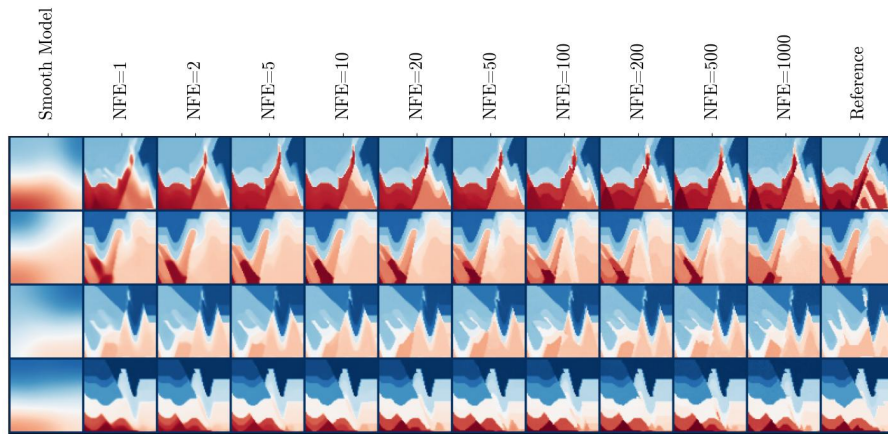
Figure 8: Performance comparison for introduced frameworks with different sets of hyperparameters. Setting a higher value of loss weighting factor w for cI²SB is beneficial for inference in purely conditional mode (solid line with diamond markers for $w_{\text{cond}} = 10$, dashed line with diamond markers for $w_{\text{cond}} = 0$)



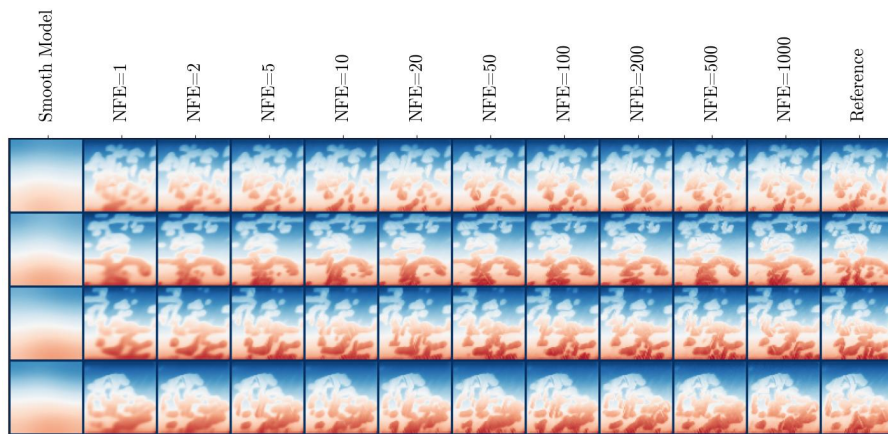
(a) CurveVel.B



(b) FlatFault.B



(c) CurveFault.B



(d) Style.B

Figure 9: Velocity models reconstructed with cl^2SB for varying number of NFEs



Figure 10: Reconstructed velocity model slices for varying number of NFEs

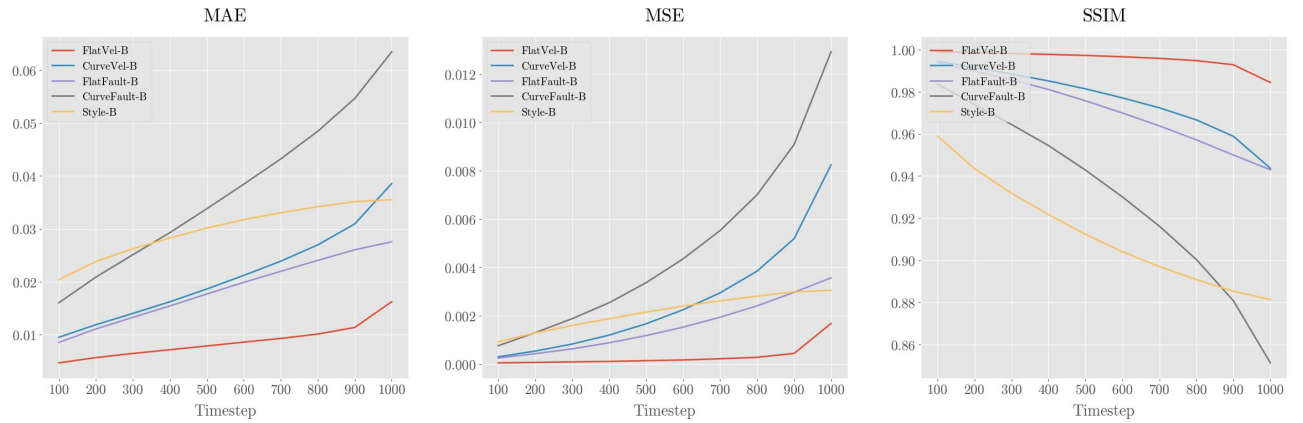
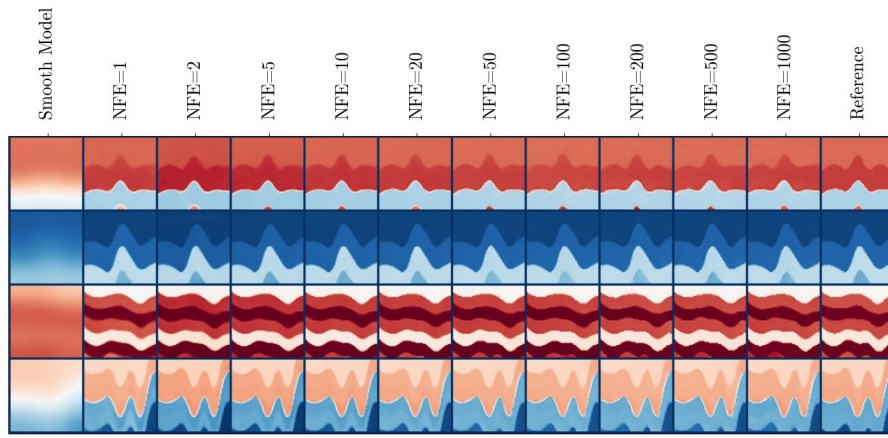
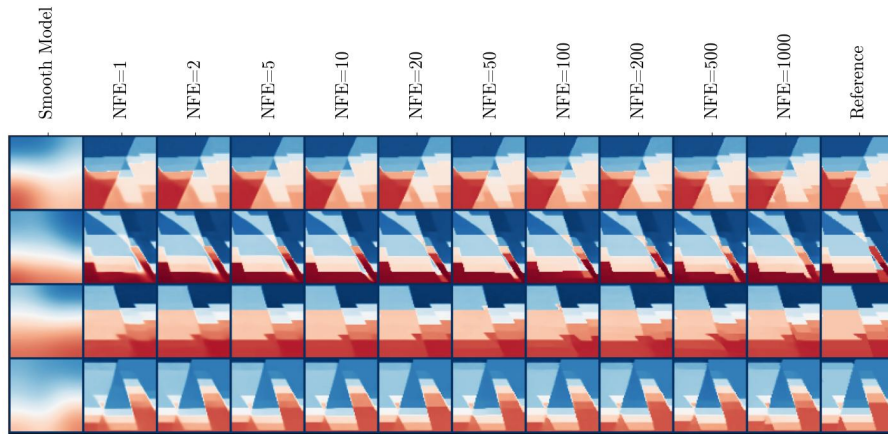


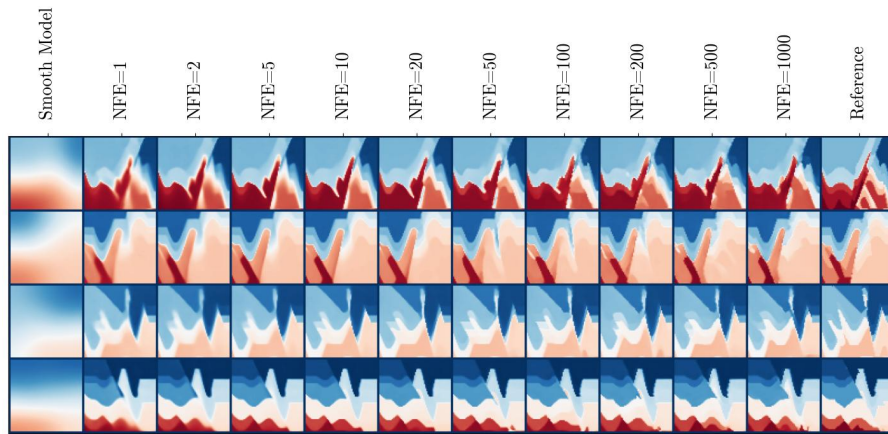
Figure 11: Dependency of validation metrics from timestep n for single-point estimates with `ci2sb-seismic-large` model given the point \mathbf{c}_n from bridge (17) and timestep value.



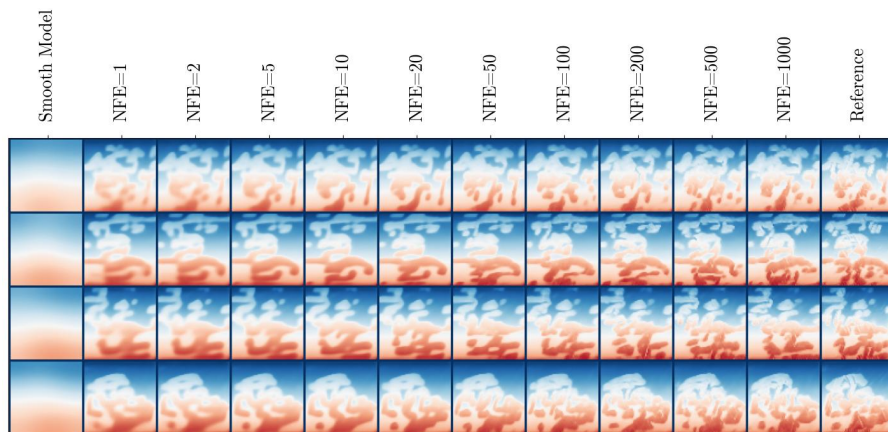
(a) CurveVel_B



(b) FlatFault_B



(c) CurveFault_B



(d) Style_B

Figure 12: Velocity model reconstructed with cSGM for varying number of NFEs

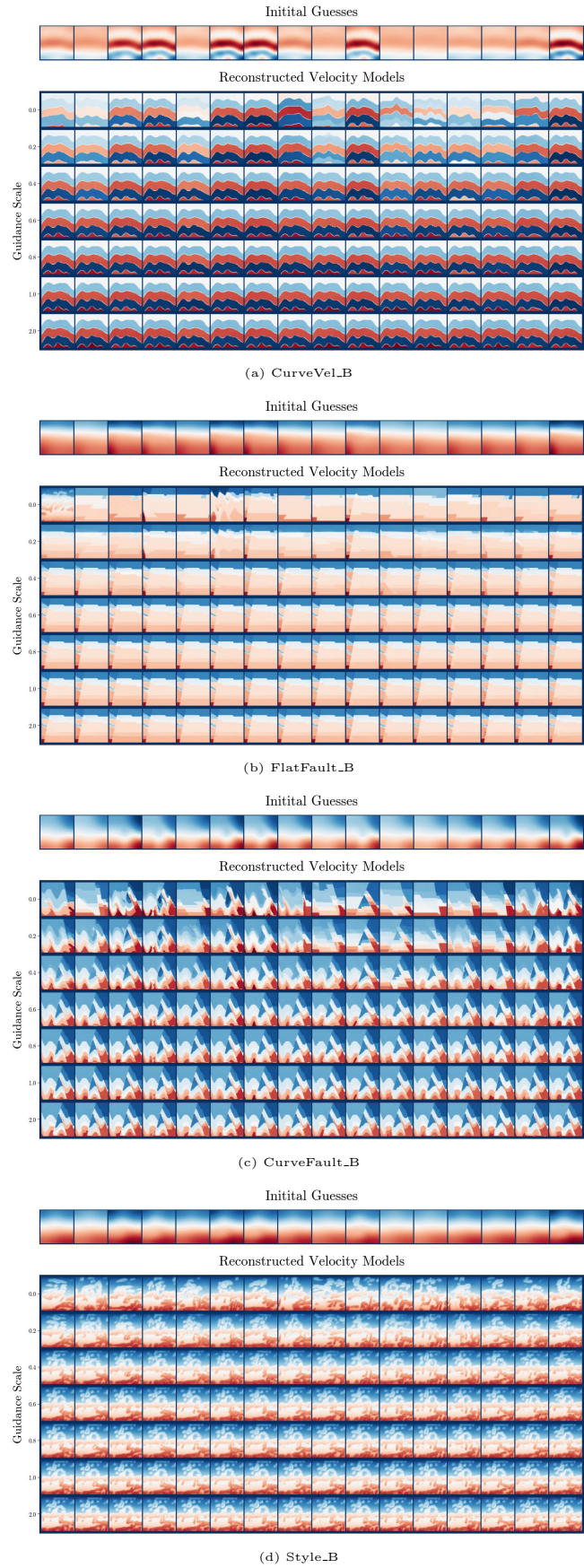


Figure 13: Velocity models reconstructed with cI^2SB for varying values of guidance scale